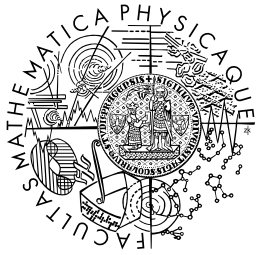

FACULTY
OF MATHEMATICS
AND PHYSICS
Charles University

MASTER THESIS

Olga Rybakova

Anisotropic Optical Properties of Fluorescent Proteins

Institute of Physics of Charles University

Supervisor of the master thesis: Josef Lazar, Ph.D.
Study programme: Physics
Study branch: Biophysics and chemical physics

Prague 2020

I declare that I carried out this master thesis independently, and only with the cited sources, literature and other professional sources. It has not been used to obtain another or the same degree.

I understand that my work relates to the rights and obligations under the Act No. 121/2000 Sb., the Copyright Act, as amended, in particular the fact that the Charles University has the right to conclude a license agreement on the use of this work as a school work pursuant to Section 60 subsection 1 of the Copyright Act.

In ..... date ....

Author's signature

Acknowledgment

I would like to express my sincere gratitude to my supervisor Dr. Josef Lazar for the given opportunity and his dedicated support and guidance during my studies. I am also deeply grateful to my colleague and friend, Dr. Alex Bondar for his help with molecular biology and biochemistry experiments and continuous encouragement and support. Besides, I would like to thank Dr. Stepan Timr, who introduced me to molecular dynamics simulations and quantum mechanical calculations and with whom I consulted on the quantum mechanical calculations presented in this thesis.

In addition, my sincere thanks to my friends, Anna Lavrova and Ondrej Tichacek, for the technical support and recommendations. And the last but not least, thanks to my parents for their constant support and patience.

Title: Anisotropic Optical Properties of Fluorescent Proteins

Author: Olga Rybakova

Department: Institute of Physics of Charles University

Supervisor: Josef Lazar, Ph.D., Institute of Physics of Charles University

Abstract: Fluorescent proteins (FPs) are the workhorses of biological molecular imaging. Important imaging modalities (such as polarization microscopy or FRET imaging) exploit anisotropic optical properties of fluorescent proteins. In this thesis, we present the results of our polarization microscopy and X-ray diffraction experiments on FP crystals, as well as mathematical interpretation of these results, yielding information on the directionality of one- and two-photon absorption within the investigated fluorescent protein molecules. For the anisotropy of one-photon absorption, we determine the transition dipole moment (TDM) orientations in three representative fluorescent proteins. Validation with available quantum mechanical predictions values and an experimentally determined TDM orientation of the GFP gives confidence to the results obtained. For the two-photon absorption, we first test our hypothesis that two-photon absorptivity tensors of representative FPs exhibit vector-like behaviour and then examine the applicability of this simplification as a basis for the interpretation of our two-photon polarization microscopy data.

Keywords: fluorescent protein, transition dipole moment, two-photon absorptivity tensor

Abstrakt: Fluorescenční proteiny (FP) jsou velice důležité pro moderní biologické molekulární zobrazování. Důležité zobrazovací techniky (jako je polarizační mikroskopie nebo FRET zobrazování) využívají anisotropických optických vlastnosti fluorescenčních proteinů. V této práci prezentujeme výsledky polarizační mikroskopie a rentgenových difrakčních experimentů na krystalech FP, jakož i matematickou interpretaci těchto výsledků, poskytující informace o směrovosti jedno- a dvoufotonové absorpce v rámci molekul zkoumaných fluorescenčních proteinů. Pro anizotropii jenofotonové absorpce určujeme orientaci dipólových momentů přechodu ve třech reprezentativních fluorescenčních proteinech. Porovnání naměřených hodnot s dostupnými kvantově-mechanickými předpověďmi a experimentálně stanovenou orientací dipólového momentu přechodů GFP nám dává důvěru k získaným výsledkům. Pro dvoufotonovou absorpci nejprve testujeme naši hypotézu, že tenzory dvoufotonové absorptivity reprezentativních FP vykazují vektorové chování. Dále pak zkoumáme použitelnost tohoto zjednodušení jako základ pro interpretaci našich mikroskopických dat dvoufotonové polarizace.

Klíčová slova: fluorescenční protein, dipólový moment přechodu, tenzor dvoufotonové absorpce

Contents

1 Introduction **3**
- 1.1 Molecular fluorescence . . . 3
- 1.2 Fluorescent proteins . . . 4
  - 1.2.1 Discovery of fluorescent proteins . . . 4
  - 1.2.2 Structure of the Green Fluorescent Protein . . . 5
  - 1.2.3 Structure of studied fluorescent proteins . . . 5
  - 1.2.4 Use of fluorescent proteins in life sciences . . . 8
  - 1.2.5 Anisotropic optical properties of fluorescent proteins . . . 8
  - 1.2.6 Fluorescent protein crystals . . . 9
- 1.3 One-photon absorption . . . 10
- 1.4 Two-photon absorption . . . 11
- 1.5 Study goals . . . 14

2 Methods **15**
- 2.1 Protein purification and crystallization . . . 15
- 2.2 X-ray diffraction measurements . . . 17
- 2.3 Polarization microscopy measurements . . . 18
- 2.4 Quantum mechanical calculations . . . 20
- 2.5 Mathematical modelling . . . 20

3 Results **24**
- 3.1 Structural and orientational information on FPs crystals . . . 24
- 3.2 Polarization microscopy measurements on FPs crystals . . . 26
  - 3.2.1 One-photon polarization microscopy . . . 26
  - 3.2.2 Two-photon polarization microscopy . . . 28
- 3.3 Analysis of experimental data in terms of TDM orientations . . . 30
  - 3.3.1 Uneven light penetration . . . 32
  - 3.3.2 Multiple solutions . . . 37
- 3.4 Vector-like behaviour of 2P absorption in studied FPs . . . 39
- 3.5 Analysis of experimental data in terms of MARV orientations . . . 40
  - 3.5.1 Multiple solutions . . . 40
- 3.6 Final results . . . 42

4 Discussion **44**

5 Conclusion **45**

Bibliography **46**

List of Abbreviations **49**

List of Figures **50**

List of Tables **51**

A Attachments **52**
A.1 Values of $\boldsymbol{r_{exp}^{1P}}$ obtained for individual crystals 52
A.1.1 mTurquoise FP 52
A.1.2 eGFP 54
A.1.3 mCherry FP 55
A.2 Values of $\boldsymbol{r_{exp}^{2P}}$ obtained for individual crystals 56
A.3 Optimized fluorophores coordinates of studied FPs 57
A.3.1 mTurquoise FP 57
A.3.2 eGFP 58
A.3.3 mCherry FP 59
A.4 Examples of Wolfram Mathematica code 60
A.5 Non-fluorescent mutant of mTurquoise FP 62
A.6 Additional X-ray diffraction measurements 64

1. Introduction

1.1 Molecular fluorescence

Molecular fluorescence is the emission of visible light by a molecule upon absorption of visible or invisible electromagnetic radiation. Molecules are known to take on certain discrete values of energy, called energy levels. The lowest possible electronic energy state of a molecule is called the ground state.

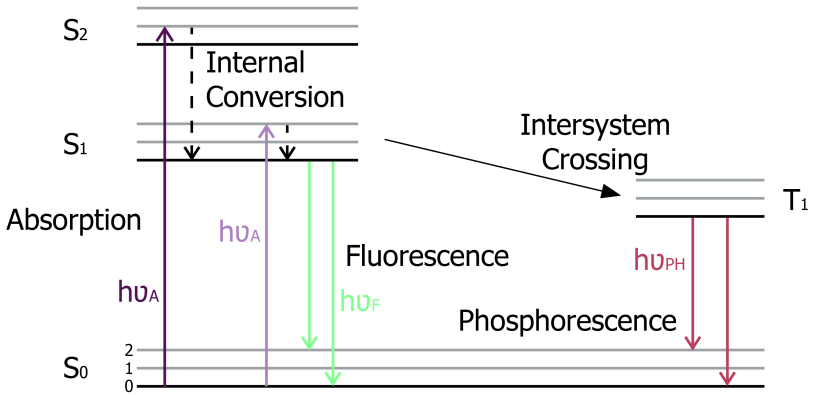

Figure 1.1: A version of Jablonski diagram. Electronic energy levels (S_0, S_1, S_2, T_1) are shown in black, their corresponding vibrational levels are shown in grey. Violet arrows represent energy changes upon transition of a molecule from the ground energy level to higher excited states associated with an absorption of a photon with energy $h\nu_A$. Green arrows represent system transition from the first singlet excited state S_1 to the ground state S_0 associated with an emission of a photon with energy $h\nu_F$ (fluorescence) and red arrows represent system transition from the first triplet excited state T_1 to the ground state S_0 associated with an emission of a photon with energy $h\nu_{PH}$ (phosphorescence).

When a molecule in a singlet ground electronic state S_0 absorbs electromagnetic radiation, it can be excited to a higher electronic energy state S_n, as well as change its vibrational state. These transitions occur in about 10^{-15} s. For most molecules upon excitation, the excess energy rapidly (in about 10^{-12} s or less) dissipates, and molecules end up in the lowest vibrational level of the first excited electronic state S_1. This process is called internal conversion. The following transition of a molecule from S_1 back to the ground state S_0 (in about 10^{-8} s or less) is called fluorescence. Molecules in the S_1 state can also undergo a spin conversion to the first triplet state T_1. This transition is called system crossing. Following transition of a molecule from T_1 to S_0 state is forbidden. This caused the rate of phosphorescence (emission from T_1) to be several orders of magnitude smaller than those for fluorescence. Phosphorescence is generally shifted to longer wavelengths relative to the fluorescence and has a corresponding lifetime of about 10^{-6} s. An illustration is given by a Jablonski diagram (see Figure 1.1) Lakowicz [2006].

1.2 Fluorescent proteins

Fluorescent proteins (FPs) are members of a group of proteins with a unique property of being self-sufficient to form a visible wavelength fluorophore from a sequence of three amino acids within their own polypeptide chain. It is common research practice for biologists to introduce a gene encoding an appropriately modified FP into living cells and visualize the location and dynamics of the FP using fluorescence microscopy Campbell [2008].

1.2.1 Discovery of fluorescent proteins

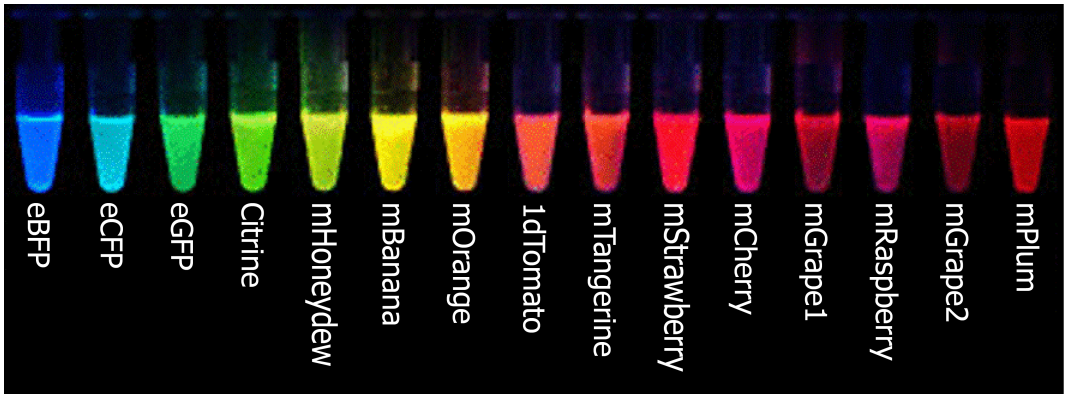

Figure 1.2: A few examples of spectrally different FP (image courtesy of R.Tsien lab).

The Green Fluorescent Protein (GFP) was first purified from the jellyfish Aequorea victoria in 1962 by Osamu Shimomura. Three decades later, in 1992, Douglas Prasher successfully cloned and sequenced the gene encoding the GFP and proposed to use GFP as a tracer molecule in living cells. In 1994, the laboratory of Martin Chalfie at Columbia University succeeded in heterologous expression of GFP in Caenorhabditis elegans (C. elegans) and provided the very first application of GFP. In 1995, a 37 °C folding efficiency point mutant was discovered in 1995 by the laboratories of Thastrup and Falkow, yielding enhanced GFP (eGFP), a fluorescent protein with increased fluorescence, photostability with respect to the original, wild-type GFP (wtGFP). eGFP allowed the practical use of GFPs in mammalian cells. GFP has then been adapted to identify fluorescent markers in other spectral regions. In 1999, a first red GFP-like fluorescent protein was purified by Sergey A. Lukyanov from the coral Discosoma sp. (the DsRed FP). Later on other wild-type FP variants such as yellow fluorescent protein (YFP) and cyan fluorescent protein (CFP) were discovered in Anthozoa. By introducing various mutations into the wild-type FPs, many other FP variants have been made, allowing for better practical biological applications. Among those are also spectral FP variants, with their emission/excitation spectra shifted with respect to the original, wild-type proteins (see Figure 1.2).

1.2.2 Structure of the Green Fluorescent Protein

The GFP molecule consists of a β-barrel composed of eleven β-sheets with the fluorophore buried inside the barrel. The fluorophore of GFP (CRO) consists of a 4-(p-hydroxybenzylidene)-imidazolidin-5-one structure spontaneously arising by a cyclization and oxidation reaction from three amino acids (Ser-Tyr-Gly) of the polypeptide chain. The non-modified Ser-Tyr-Gly tripeptide is not fluorescent by itself and can be found in many proteins not showing any fluorescence properties. Prasher et al. [1992] Fang et al. [2009] The structure of wtGFP (PDB: 1EMB) as well as corresponding absorption and emission spectra are present in the Figure 1.3.

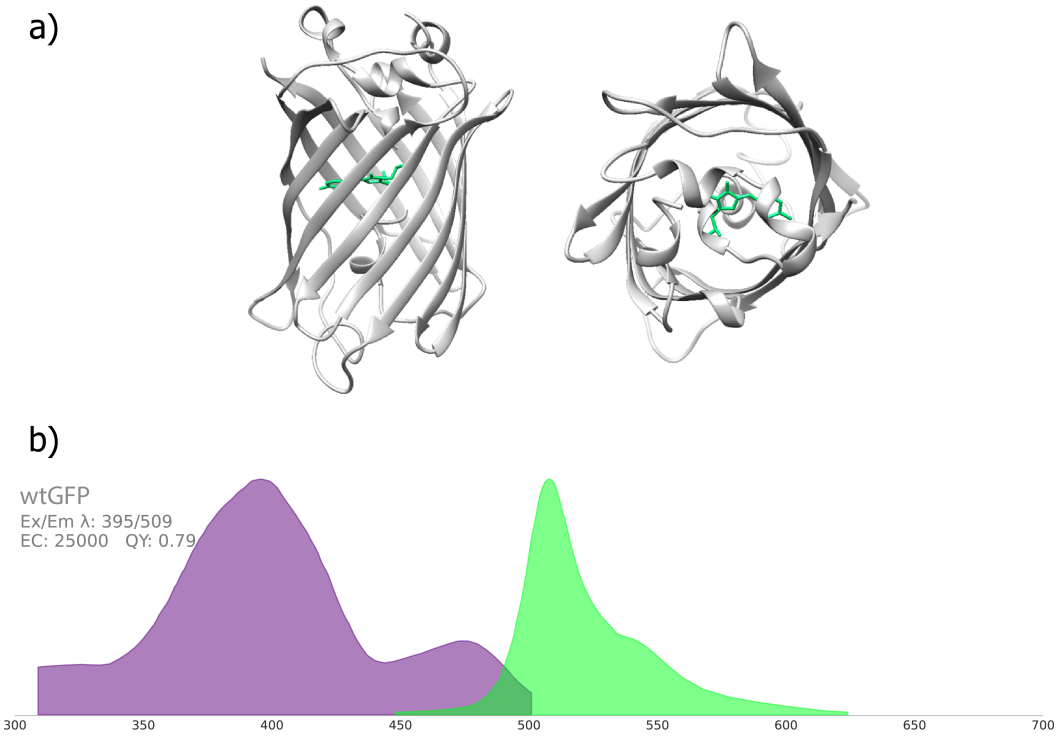

Figure 1.3: a) Structure of wtGFP (PDB: 1EMB). The β-barrel structure is shown in grey in ribbon format. The fluorophore (CRO) is shown in green (illustration is made using Chimera software). b) Absorption and emission spectra of wtGFP. Maximum of wtGFP excitation is at 395 nm wavelength, and the maximum of wtGFP emission is at the 509 nm wavelength (spectra image is taken from www.fpbase.org).

1.2.3 Structure of studied fluorescent proteins

Studied absorption and emission properties of FPs are determined by amino acids forming the fluorophore as well as by their surrounding amino acids. Mutations in these amino acids may lead to changes in excitation and emission spectra as well as in other photochemical properties, such as photostability and quantum yield. Nowadays a whole range of FPs with excitation and emission spectra spanning from ultraviolet to infrared is available for biological applications. In this thesis, we have studied three representative FPs that are widely used in a

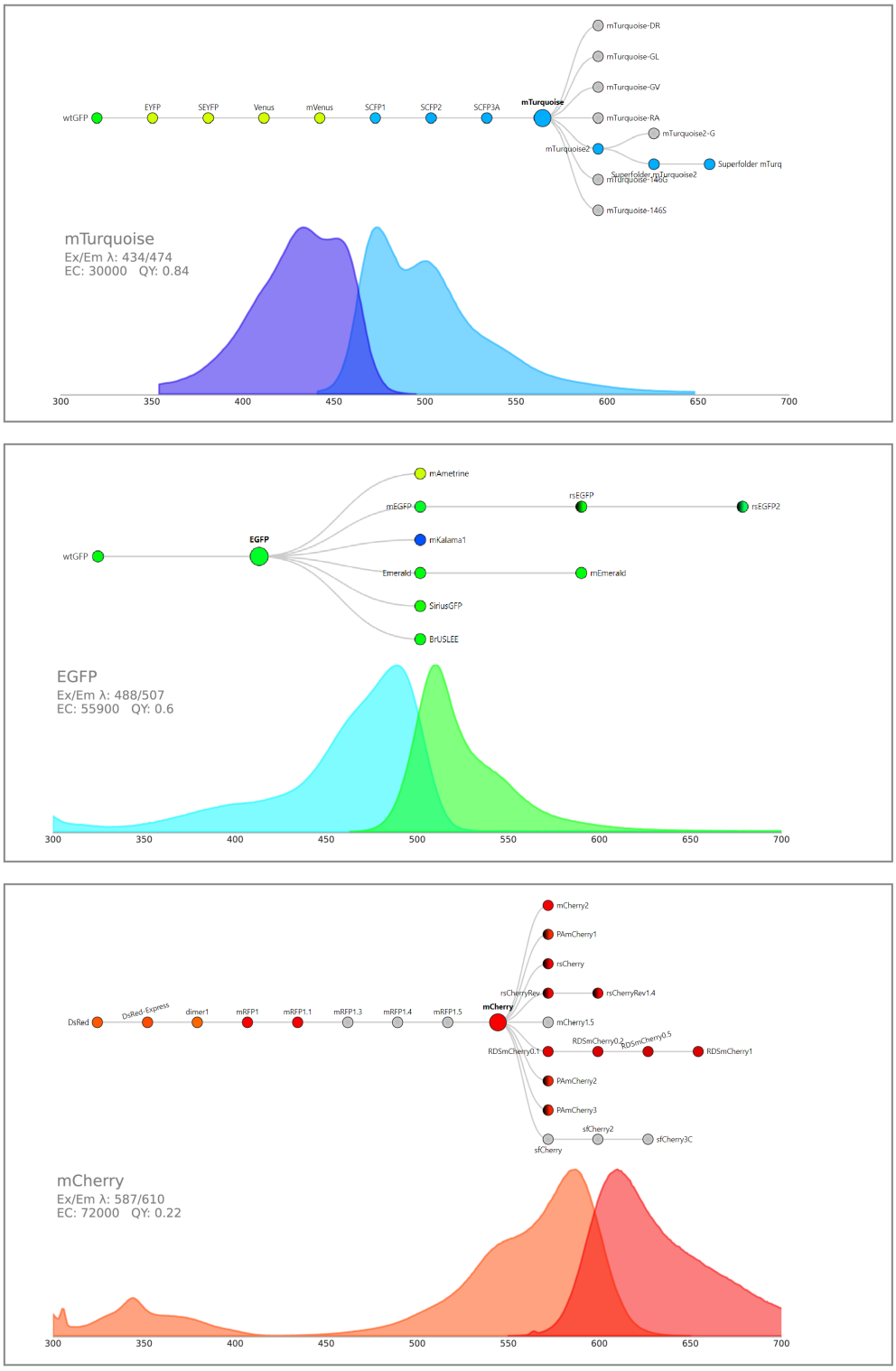

Figure 1.4: Information on the three studied FPs. Schemes show that both mTurquoise (PDB: 4AR7) and eGFP (PDB: 2Y0G) are the derivatives of the wtGFP and mCherry (PDB: 2H5Q) is a derivative of the DsRed FP. Maximum of mTurquoise excitation is at 434 nm wavelength, maximum of emission is at 474 nm wavelength. The molar attenuation coefficient of mTurquoise is 30 000 $M^{-1}cm^{-1}$. Maximum of eGFP excitation is at 488 nm wavelength, maximum of emission is at 507 nm wavelength. Maximum of mCherry excitation is at 587 nm wavelength, maximum of emission is at 610 nm wavelength (Images obtained at www.fpbase.org).

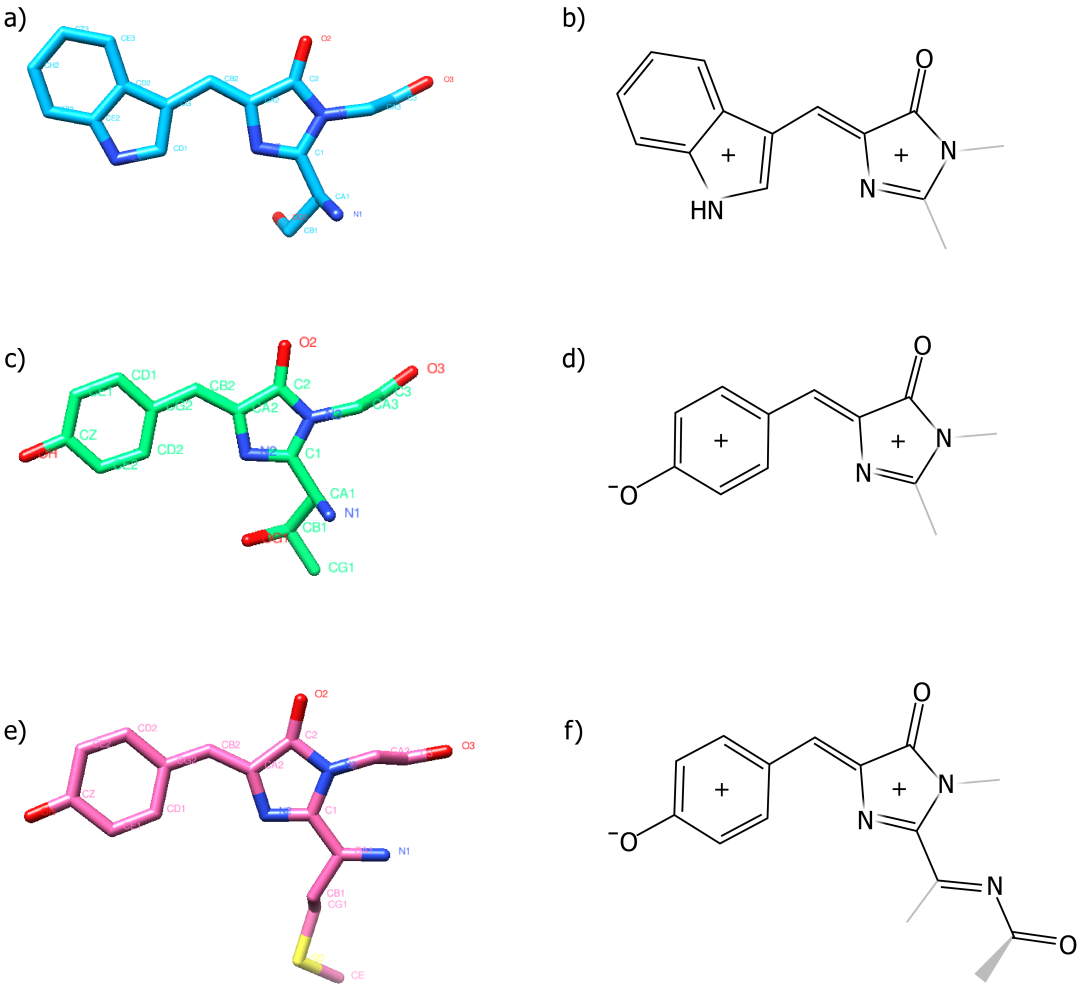

Figure 1.5: Fluorophores of the three studied FPs are shown. The fluorophore of mTurquoise, SWG, is formed by spontaneous cyclization and oxidation of three amino acids (Ser-Trp-Gly) of the polypeptide chain. eGFP fluorophore, CRO, is the same as of the wtGFP, and is formed by cyclization and oxidation of Ser-Tyr-Gly amino acids. mCherry fluorophore, CH6, is formed by cyclization and oxidation of Met-Tyr-Gly amino acids. Images a), c), e) show 3D structure of the mTurquoise, eGFP and mCherry fluorophores respectively. Oxygen atoms are coloured in red, nitrogen – in blue, sulphur – in yellow, carbon chains are coloured accordingly to the fluorophore's emission wavelength for illustration purposes (illustrations are made using Chimera software). Images b), d), f) schematically represent systems of conjugated double bonds of mTurquoise, eGFP and mCherry FP fluorophores respectively. Black crosses represent centres of the rings. Note that for mCherry fluorophore, CH6, the part containing sulphur is omitted as it is not a part of the conjugated double-bond system, and the carbon and oxygen atoms from a neighbouring residue, Phe65, are included. Those schemes were build according to Ansbacher et al. [2012]. These exact schemes were used for QM calculations of 2PATs of studied FPs. Note that in light grey colour are shown parts of the structures which were omitted at calculations of approximating planes of fluorophores.

broad spectrum of optical microscopy techniques: mTurquoise (a cyan FP derived from wtGFP) Goedhart et al. [2010], eGFP (a green FP derived from wtGFP) Cormack et al. [1996] and mCherry (a red FP derived from DsRed) Shaner et al. [2004]. For their absorption and emission spectra as well as their relation to the original, wild-type FPs see Figure 1.4.

Fluorophores of all FPs derived from GFP and coral FPs are almost planar asymmetric systems forming a chain of conjugated double-bonds Ansbacher et al. [2012]. In the Figure 1.5 we show spatial images of fluorophores of the three studied representative FPs, as well as their corresponding planar schemes illustrating conjugated double-bond systems participating in absorption Ansbacher et al. [2012]. Note that for mCherry fluorophore, CH6 (Met-Tyr-Gly), the part containing sulphur is omitted as it is not a part of the conjugated double-bond system, and the carbon and oxygen atoms from a neighbouring residue, Phe65, are included.

1.2.4 Use of fluorescent proteins in life sciences

In the years since their discovery, FPs have become an indispensable tool of a vast variety of biological imaging techniques.The main reason for using FPs over other fluorescent tags in biological applications is that a FP fluorophore forms in the live organisms without the need for any cofactor (other than molecular oxygen), and hence can be used as genetically encoded fluorescent probes in studying cellular processes in living cells. At the same time, FPs are relatively small in size (c. 30 kDa).

Since the discovery of GFP, many FP variants have been developed Rodriguez et al. [2017], with various properties that have allowed an ever-expanding range of applications in biological imaging Germond et al. [2016]. Development of colour variants (ranging from ultraviolet to near infrared) has opened the door to simultaneous imaging of multiple molecular processes. Using suitable pairs of FPs has allowed measuring molecular distances by using Förster resonance energy transfer (FRET). Increase of pH sensitivity has allowed sensitive imaging of pH changes in cells. Engineering FPs with various excited state lifetimes has allowed imaging of changes in molecular environment. Photoswitchable FPs (FPs that change their colour upon illumination by light of a particular wavelength) have allowed tracking of individual FP molecules and imaging with spatial resolution better than the diffraction limit of optical microscopy. This has allowed imaging of many molecular processes.

1.2.5 Anisotropic optical properties of fluorescent proteins

Since the early days of FP use, when FPs were used as simple reporters of protein expression and localization, ever more sophisticated applications of FPs for studying cellular processes have been developed. Various optical properties of FPs have allowed visualizing many molecular processes in living cells and organisms. Of increasing importance for biological imaging have been the anisotropic optical properties of FPs. Absorption of a photon causes an initial alleviation of a conjugated double bond chain in the fluorophore. The directionality of this

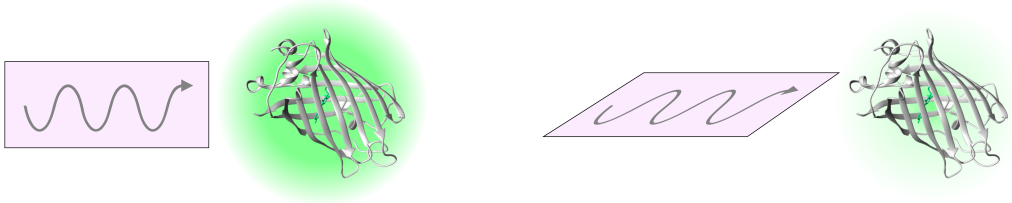

Figure 1.6: Optical properties of FPs are anisotropic: probability of absorption of a photon depends on the orientation of the FP molecule with respect to polarization of the excitation light.

process makes FPs sensitive to the polarization of the excitation light. The rate of light absorption (and hence fluorescence) by FP molecules depends on their orientation with respect to the polarization of the incoming light (see Figure 1.6). The direction and polarization of fluorescent emission also depends on FP molecular orientation. This orientational dependence is important in fluorescence polarization imaging, in interpreting FRET results Piston and Kremers [2007], Khrenova et al. [2015], and in fluorescence detected linear dichroism (FDLD) imaging Lazar et al. [2011]. In order to quantitatively interpret results obtained by these methods, it is crucial to understand the anisotropic properties of fluorescent proteins.

1.2.6 Fluorescent protein crystals

Under favourable conditions FPs tend to form crystals, i.e. stable structures of known molecular orientation. In contrast to FP solution, where all FP orientations are equally distributed, in FP crystal FPs are oriented along just several, well-defined directions. FP crystals of sufficient size can be measured on X-ray diffractometer, therefore the corresponding FP structure as well as the characteristic FP orientations can be determined (see Figure 1.7). This along with the fact that the rate of absorption of FP depends on its orientation with respect to the polarization of the excitation light makes crystals of FPs a suitable system for studying directionality of light absorption.

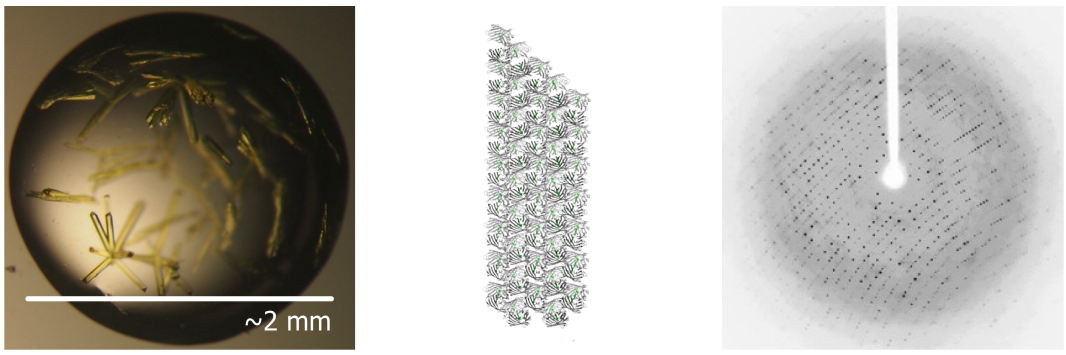

Figure 1.7: FP crystals allow for structural and orientational analysis. a) An image of a crystallization drop containing eGFP crystals. b) A schematic representation of FP molecules orientations within a FP crystal in P212121 space group (illustration is made in Chimera software). c) An example of Laue diffractogram of crystal in P212121 space group.

1.3 One-photon absorption

An ordinary absorption process involves a single photon (for Jablonski diagram of one-photon (1P) absorption and following fluorescent emission see Figure 1.8).

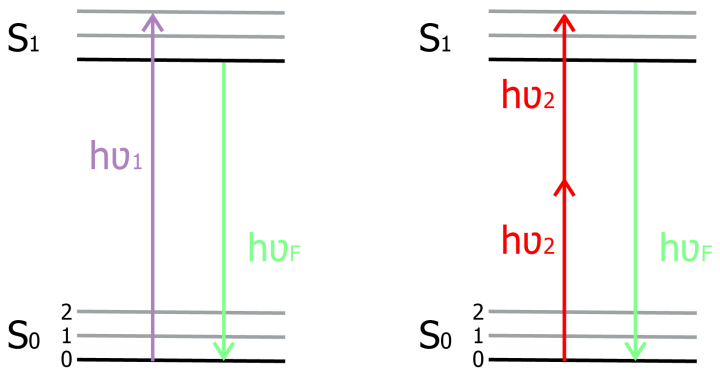

Figure 1.8: Jablonski diagram illustrating 1P versus 2P absorption by a molecule and the following fluorescence emission. In case of 1P absorption (left), one photon with wavelength λ_1, frequency ν_1 and energy $h\nu_1$ is absorbed. In case of 2P absorption (right), a virtually simultaneous absorption of two photons with wavelength $\lambda_2 = 2\lambda_1$, frequency $\nu_2 = \frac{\nu_1}{2}$ and energy $h\nu_2 = \frac{h\nu_1}{2}$ occurs. Absorption is followed by emission of a photon with energy $h\nu_F$.

The rate of 1P absorption of incident light by a molecule R^{1P} is proportional to the intensity of the excitation radiation I with a coefficient σ^{1P}, called the 1P absorption cross section:

$$R^{1P} = \sigma^{1P} I \tag{1.1}$$

In case of absorption of linearly polarized light, the cross section of 1P absorption is proportional to the second power of cosine of the angle φ between the electric field polarization vector $\vec{e}$ and a vector $\vec{\mu}$ corresponding to the molecule's transition from a ground to an excited state, the so-called transition dipole moment (TDM) (see Figure 1.9):

$$\sigma^{1P} \sim (\vec{e} \cdot \vec{\mu})^2 \sim \cos^2 \varphi. \tag{1.2}$$

Therefore, a fluorescent molecule absorbs light polarized parallel to the excitation TDM and does not absorb light polarized perpendicularly to the TDM.

Although knowing the molecular orientations of TDMs allows for quantitative interpretation of many imaging experiments in terms of protein structure, almost no published information on directions of TDMs obtained by measurements on FPs molecules is available. Thus, as far as we know, only the orientation of the 410 nm excitation TDM of GFP has been determined Fang et al. [2009]. Although some information on FPs TDMs orientations can be gleaned from measurements and calculations on model compounds Ansbacher et al. [2012], results obtained on model compounds are of limited value, since spectroscopic properties of the FPs fluorophores are known to be heavily affected by the molecular environment of the fluorophore. Shu et al. [2006].

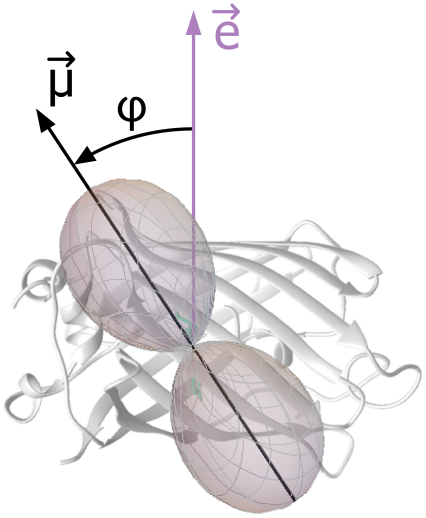

Figure 1.9: A schematic representation of orientational dependence of rate of 1P absorption by a FP molecule. A TDM $\vec{\mu}$ is associated with FP's fluorophore. The grey cloud represents 1P absorption cross section σ^{1P}. The rate of absorption of a linearly polarized light with an electric field vector $\vec{e}$ by a FP molecule with a given TDM orientation $\vec{\mu}$ is proportional to $\cos^2 \varphi$.

1.4 Two-photon absorption

A process of virtually simultaneous absorption of multiple photons of light by a molecule followed by the promotion of the molecule from a ground state to an excited electronic state is called multiphoton absorption Ustione and Piston [2011]. In this thesis we are studying the anisotropy of absorption of two photons at a time, the so-called two-photon (2P) absorption (see Figure 1.8).

In contrast to 1P absorption rate R^{1P}, 2P absorption rate R^{2P} is proportional to the second power of the intensity of the excitation radiation I:

$$R^{2P} = \frac{1}{2}\sigma^{2P} I^2, \tag{1.3}$$

where σ^{2P} is the 2P absorption cross section, that gives the propagability of simultaneous absorption of two photons with their total energy matching the energy of molecular transition from the ground to an excited electric energy state Drobizhev et al. [2011]. In contrast to 1P absorption, 2P absorption is a nonlinear optical process. The rate of 2P absorption is given by the double projection of two electric field vectors $\vec{e}$ onto a molecular second-rank tensor $\underline{\underline{S}}$, the 2P absorptivity tensor (2PAT) (see Figure 1.10) Lakowicz [1991]:

$$\sigma^{2P} \sim (\vec{e} \cdot \underline{\underline{S}} \cdot \vec{e})^2. \tag{1.4}$$

Considering that $\{S_i\}_{i=1}^3$ are the eigenvalues and $\{\vec{s}_i\}_{i=1}^3$ are the corresponding eigenvectors of $\underline{\underline{S}}$, we can rewrite Equation 1.4 in the following way:

$$\sigma^{2P} \sim (\sum_{i=1}^{3} S_i (\vec{e} \cdot \vec{s}_i)^2)^2. \tag{1.5}$$

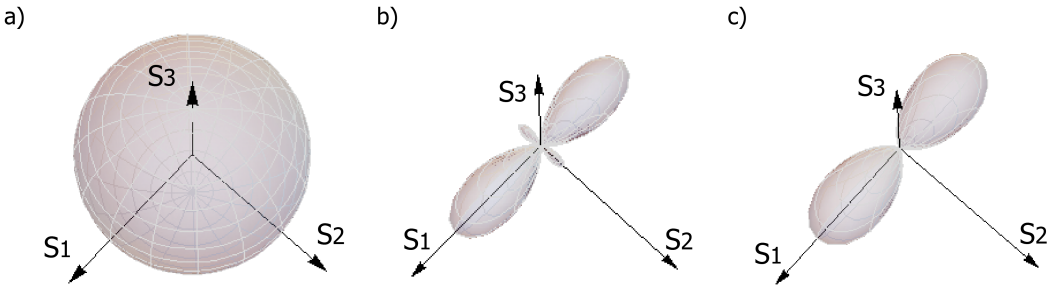

Figure 1.10: Graphs of possible 2P absorption cross section shapes for absorption of two identical linearly polarized photons. The distance to the surface from the origin gives the rate of absorption. $\{\vec{s}_i\}_{i=1}^{3}$ are the 2PAT eigenvectors. Image a) shows the shape and the orientation of the 2P absorption cross section when (S_1, S_2, S_3) are proportional to $(1, 1, 1)$ – anisotropic scenario. Image b) shows the shape and the orientation of the 2PA cross section when (S_1, S_2, S_3) are proportional to $(1, -\frac{1}{2}, 0)$ and c) – when (S_1, S_2, S_3) are proportional to $(1, 0, 0)$, i.e. when there is a single prevalent eigenvalue of 2PAT. In that case the shape of 2P absorption cross section becomes similar to the shape of 1PA cross section and the directionality of 2P absorption can be described just by the eigenvector $\vec{s}_1 \equiv \vec{\mu}^{2P}$, the Maximum Absorption Rate Vector.

Directional properties of 2P absorption are generally complex. However, it has been shown that for some molecules (when the direction of a change in permanent dipole moment during excitation is close to the direction of the 1P TDM, for example, in rod-shaped molecules. Sy and Bw [1993], Timr et al. [2015]) 2PATs have only one dominant eigenvalue $S_1 \gg S_2, S_3$ (see Figure 1.10 c). In that case Equation 1.5 gets replaced by:

$$\sigma^{2P} \sim (S_1(\vec{e} \cdot \vec{s}_1)^2)^2 \sim (\vec{e} \cdot \vec{s}_1)^4 \sim (\vec{e} \cdot \vec{\mu}^{2P})^4 \sim \cos^4 \varphi, \tag{1.6}$$

where $\vec{s}_1 \equiv \vec{\mu}^{2P}$, the so-called Maximum Absorption Rate Vector (MARV), and φ is the angle between the MARV $\vec{\mu}^{2P}$ and an electric field vector $\vec{e}$ (see Figure 1.11). Therefore, when 2PAT tensor has only one prevalent eigenvalue, the rate of 2P absorption becomes proportional to the cosine to the fourth of the angle between the orientation of the polarization of excitation light and the MARV. That in turn means that 2P anisotropic properties of such molecules can be described by a vector rather than a tensor.

2P absorption is known to occur when the intensity of the incident light is sufficiently high. Powerful femtosecond infrared lasers are used for 2P excitation, and the 2P excitation occurs only in a small volume around the focal point within a sample. Infrared light used for 2P excitation undergoes limited scattering and allows deep tissue imaging, improved optical sectioning and limited photobleaching of a sample. This makes 2P excitation an extremely popular tool in fluorescence imaging.

Despite its importance, only little information is available on FP 2PATs. Measurements of fluorescence anisotropy of eGFP solutions indicate a relationship between the eGFP TDM direction Ansbacher et al. [2012] and the structure of

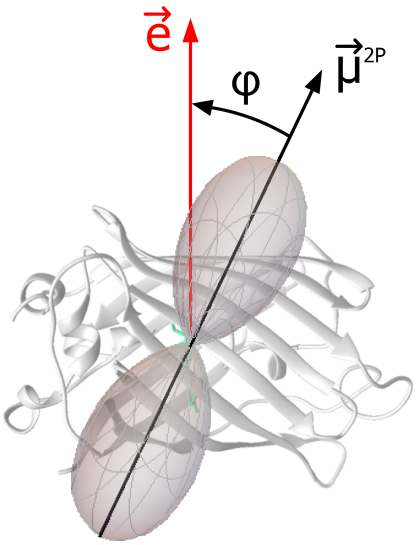

Figure 1.11: A schematic representation of orientational dependence of rate of 2P absorption by a FP molecule in case of a single dominant eigenvalue of 2PAT. A MARV $\vec{\mu}^{2P}$ is associated with FP's fluorophore. The grey cloud represents 2P absorption cross section σ^{2P} (note that its shape is more elongated and narrow than the σ^{1P} shape at the Figure 1.9). In this simplified scenario the rate of absorption of two photons of linearly polarized light with an electric field vector $\vec{e}$ by a FP molecule with a given MARV orientation $\vec{\mu}^{2P}$ is proportional to $\cos^4 \varphi$.

the 2PAT for the $S_0 - S_1$ transition Masters et al. [2018]. Comparisons of our own cell imaging results obtained with 1P and 2P excitation reveal analogies in optical behaviour of a number of FP-encoding constructs. Therefore, only very limited data on FP absorptivity tensors is available and, although circumstantial evidence points towards FP 2PATs giving rise to vector-like anisotropic optical properties, this still needs to be shown.

1.5 Study goals

In this thesis, we want to study the anisotropy of 1P and 2P absorption in three representative FPs: mTurquoise (a cyan FP), eGFP (a green FP) and mCherry (a red FP). In order to that, we plan to:

1. Obtain FPs of interest from pre-existing plasmids (using methods of molecular biology and biochemistry); obtain crystals of purified FPs.
2. With a help of our colleagues, perform X-ray diffraction measurements on obtained FP crystals in order to determine protein structure and gain information on the crystallographic unit cell orientation with respect to the FP crystal.
3. Test our hypothesis that directionality of 2P absorption of studied FPs can be described by a vector (MARV) rather than a tensor (2PAT).
4. Perform 1P and 2P polarization microscopy measurements on obtained FP crystals.
5. Analyse data obtained by X-ray diffraction and polarization microscopy measurements in terms of TDM and MARV orientations in studied FPs.

2. Methods

2.1 Protein purification and crystallization

Protein purification

To obtain FP crystals, we have first purified the studied FPs. The same procedure was used for protein purification of all three studied FPs. First, plasmids encoding FP genes were transformed into the BL21 competent *E. coli* bacterial cell line (a widely used *E. coli* expression strain suitable for transformation and protein expression) by electroporation. A 5 ml starting culture has been prepared overnight, then propagated in a larger volume (500 ml), and induced with IPTG (isopropyl β-d-1-thiogalactopyranoside, a molecular biology reagent used to induce expression of proteins with genes under the control of lac operator) for approximately 4 hours at 37 °C (a protein expression step). The expression cultures were then centrifuged, the supernatant discarded, and remaining bacteria lysed by a French press. The bacterial cell lysates were centrifuged, and the supernatants were collected and cooled.

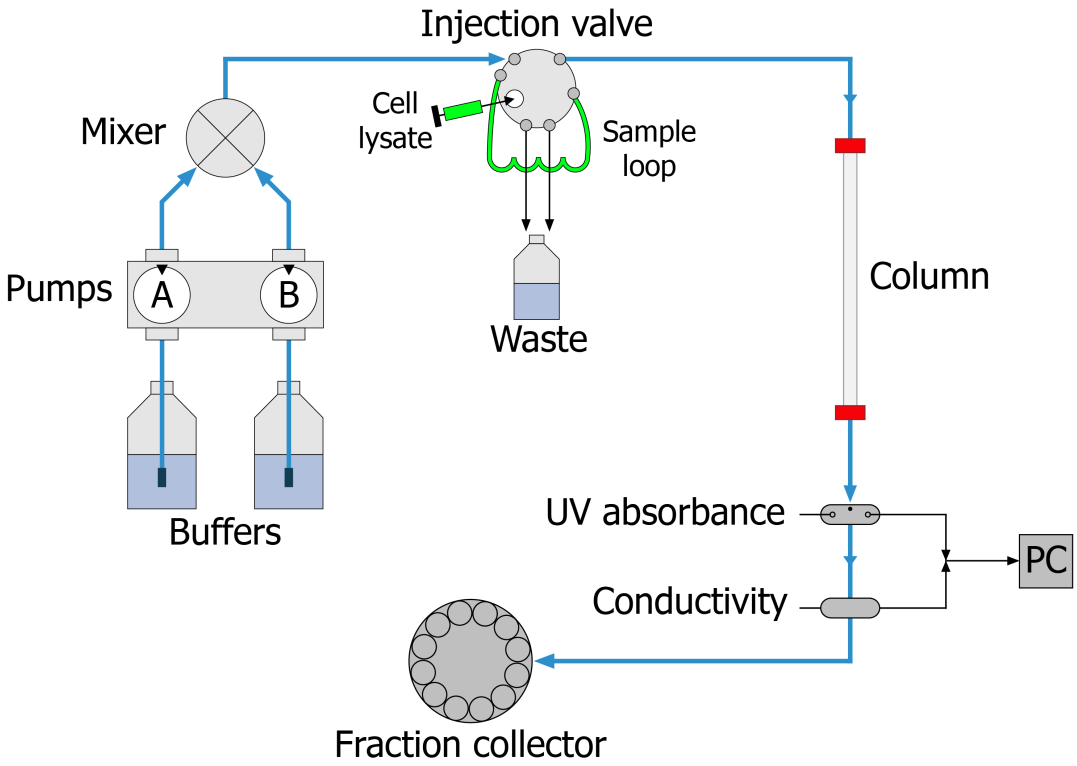

Figure 2.1: A schematic representation of ÄKTA FPLC protein purification setup used for the protein purification. Centrifuged cell lysate containing FP was loaded manually into the system via sample loop. Upon passing the HisTrap column, the UV absorbance at 280 nm wavelength has been measured in order to track protein concentration. 1 ml fractions have been collected with an automatic fraction collector.

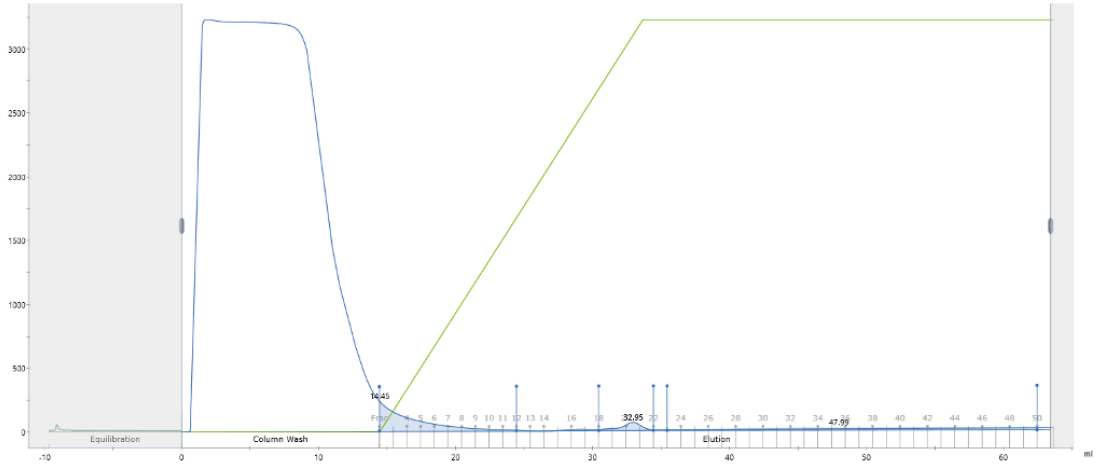

Figure 2.2: An example of a protein purification run performed on ÄKTA FPLC protein purification system. Protein concentration curve is shown in blue. Here we can see, that during the "column wash" step all proteins from the cell lysate that didn't have a histidine tag have passed through the column, while the FP of interest (with a hexahistidine tag) stayed on the column. During elution step (with a 0 % to 100 % buffer B gradient – see green line) 1 ml fractions have been collected. Here, fractions 12÷16 (presumably containing purified FP) were collected and used for further analysis and processing.

FPs (all containing a hexahistidine tag – a string of six histidine amino acids – at either the N or C terminus) were then purified by affinity chromatography on a nickel column (1 ml volume, HisTrap HP, GE Healthcare) at a 0.5 ml/min speed with a loading (A) buffer (50 mM Tris-HCl pH 7.5, 200 mM NaCl, 1 mM $MgCl_2$, 5 mM DTT, 10 mM imidazole) and a 0% to 100% gradient of wash (B) buffer (50 mM Tris-HCl pH 7.5, 200 mM NaCl, 1 mM $MgCl_2$, 5 mM DTT, 500 mM imidazole) on FPLC (ÄKTA, GE Healthcare) protein purification system. Schematic representation of the setup used in this thesis and an example of a sample run are shown in the Figures 2.1 and 2.2 respectively.

Fractions collected during the elution step were analysed by SDS-PAGE (see Figure A.2). Desired fractions have been further concentrated on Amicon Ultra-15 Centrifugal Filter Units, 30 kDa membrane NMWL in several rounds of centrifugation. Prior to crystallization, buffer composition and protein concentration have been adjusted.

Protein crystallization

All proteins have been crystallized in several rounds of crystallization at room temperature using hanging drop vapour diffusion crystallization method. All crystallizations have been set up manually with a 1 ml volume of mother liquor (ML) solution in the reservoir and a 4 µl crystallization drop (see Figure 2.3). Crystallization conditions have been varied according to the Table 2.1. Sometimes, a so-called seeding solution has been prepared out of thin, needle-like crystals and used (by adding it to a crystallization drop) as a source of nucleation origins at the next round of crystallizations.

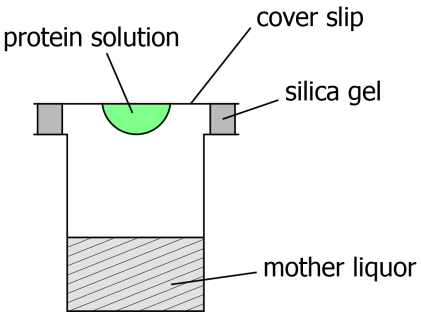

Figure 2.3: A schematic representation of hanging drop vapour diffusion crystallization method used for protein crystallization. A protein solution crystallization drop (green) has prepared on a thin quartz cover slip and attached to the reservoir containing ML solution. Connections of the cover slip with the reservoir have been sealed with a silica gel to prevent air entering the reservoir.

Table 2.1: Crystallization conditions used for crystallizations of mTurquoise, eGFP and mCherry FPs. Second column shows a final concentration of protein solution used for crystallization. Third column gives ML solution composition; for mTurquoise and eGFP FPs, the concentration of PEG¬8000 has been varied. The last column shows how the proportion of protein to ML solutions has been varied in these crystallizations. At times, a seeding solution has been added to the crystallization drop (not shown here).

FP	**FP concentration mg/ml**	**ML composition**	**protein : ML ratio in a drop**
mTurquoise	10	100 mM $MgCl_2$ 100 mM HEPES pH 6.5 15÷20 % PEG 8000	1:4 ÷ 3:4
eGFP	20	60 mM $MgCl_2$ 100 mM HEPES pH 8.0 15÷25 % PEG 8000	1:4 ÷ 3:4
mCherry	10	100 mM NaOAc 100 mM Tris pH 8.0 30 % PEG 4000	1:4 ÷ 3:4

2.2 X-ray diffraction measurements

Obtained crystals were subjected to X-ray diffraction measurements in order to verify published molecular structures and yield information on crystallographic group and orientation of main crystallographic axes within the FP crystals.

Crystals of mTurquoise and eGFP FPs were measured with the help of our colleagues from P. Rezacova group at the IOCB Prague at the in-house diffractometer setup (a MicroMax-007 HF Microfocus X-ray generator equipped with

a VariMax VHF ArcSec optical system (Rigaku, Japan), an AFC11 partial four-axis goniometer (Rigaku, Japan), a PILATUS 300K detector (Dectris, Switzerland) and a Cryostream 800 cryocooling system (Oxford Cryosystems, England)). Those measurements allowed us to verify FP structure and crystallographic space group, however were not sufficient at the time for determination of the crystallographic axes orientations with respect to the macroscopic environment. Therefore, for mTurquoise and eGFP crystals the orientation of axes with respect to the crystal was assumed to be as the one published in Rosell and Boxer [2003].

Crystals of mCherry FP were measured by our colleague A. Royant at the European Synchrotron Radiation Facility, Grenoble, France. Those measurements allowed us both the verification of the FP structure and crystallographic space group as well as the determination of the crystallographic axes orientations with respect to the macroscopic environment.

2.3 Polarization microscopy measurements

In this thesis, we have measured the dependence of fluorescence intensity of FPs crystals on the orientation of linear polarization of the excitation laser beam (denoted by vector $\vec{e}$).

Slides with crystals for polarization microscopy measurements were prepared by placing crystals of known crystallographic group in a fresh mother liquor solution in between two thin quartz cover slips sealed by an adhesive spacer. Before sealing the slides, crystals were visually checked to seat flat on these slides. Slides were then placed on a laser-scanning microscope and illuminated by a linearly polarized light of an appropriate wavelength. During acquisition, polarization of the excitation light ($\vec{e}$) was rotated within the plane of slide (xy, for the definition of coordinate system see 2.4, 2.5 and 2.7) by an achromatic half-wave plate mounted in a motorized rotating mount.

Both 1P and 2P confocal polarization microscopy measurements have been performed on a customized laser-scanning microscope based on the Olympus FV1200 confocal system, equipped with lasers for single- and two-photon excitation and a water-immersion objective lens. Excitation light was first passing through a Glan-laser calcite polariser and then through an achromatic half-waveplate installed on motorized precision rotation mount. For each crystal imaging experiment the waveplate has been rotated with a 5° increment over the 0÷360° range, changing polarization of the excitation beam by 10° each step over the 0÷720° range; at every step an image has been acquired (therefore, a total of 73 images in a single crystal measurement).

Schematic diagrams of 1P and 2P polarization microscopy setups are shown at the figures 2.4 and 2.5 respectively. In 1P polarization microscopy measurements, a short-pass dichroic mirror separated fluorescence from the excitation laser beam. Fluorescence was detected by a photomultiplier (PMT) detector (equipped with an emission filter), after passing through a confocal pinhole. In 2P polarization microscopy measurements, a long-pass dichroic mirror separated fluorescence from the excitation laser beam. For detection of fluorescence after 2P excitation the confocal pinhole positioned prior to a PMT detector has been widely open (i.e. not present).

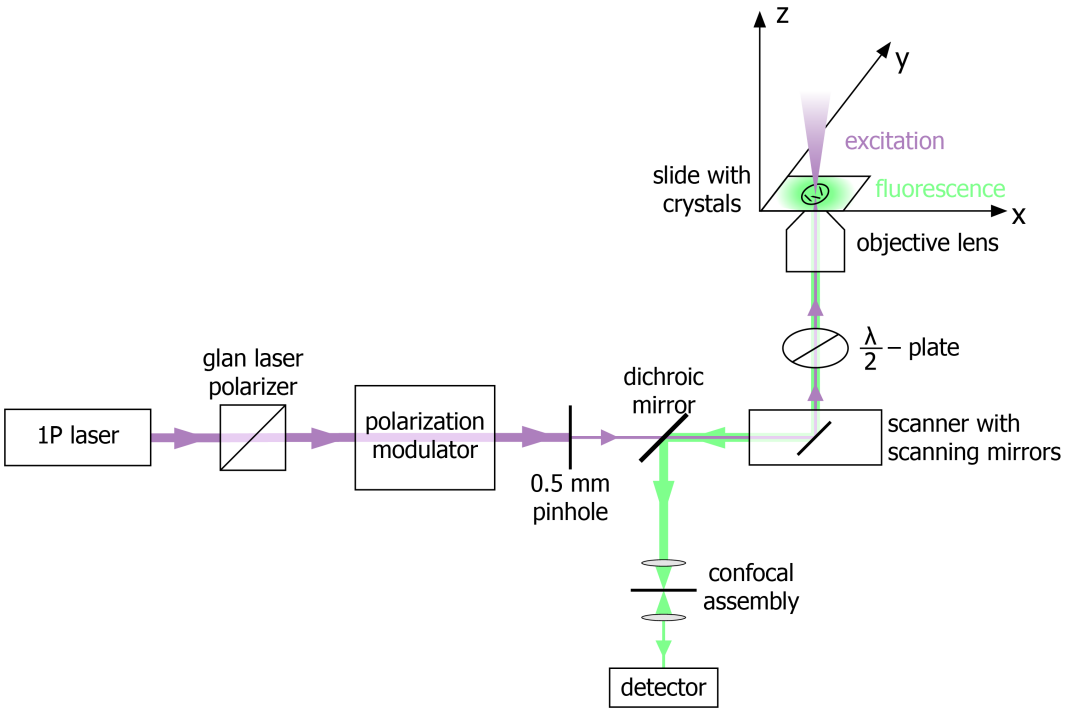

Figure 2.4: 1P polarization microscopy setup. Linear polarization of excitation light ($\vec{e}$) is rotated in the plane of the slide (plane of the crystal) xy around axis z by mechanical rotation of the achromatic half-wave plate ("$\lambda/2$–*plate*").

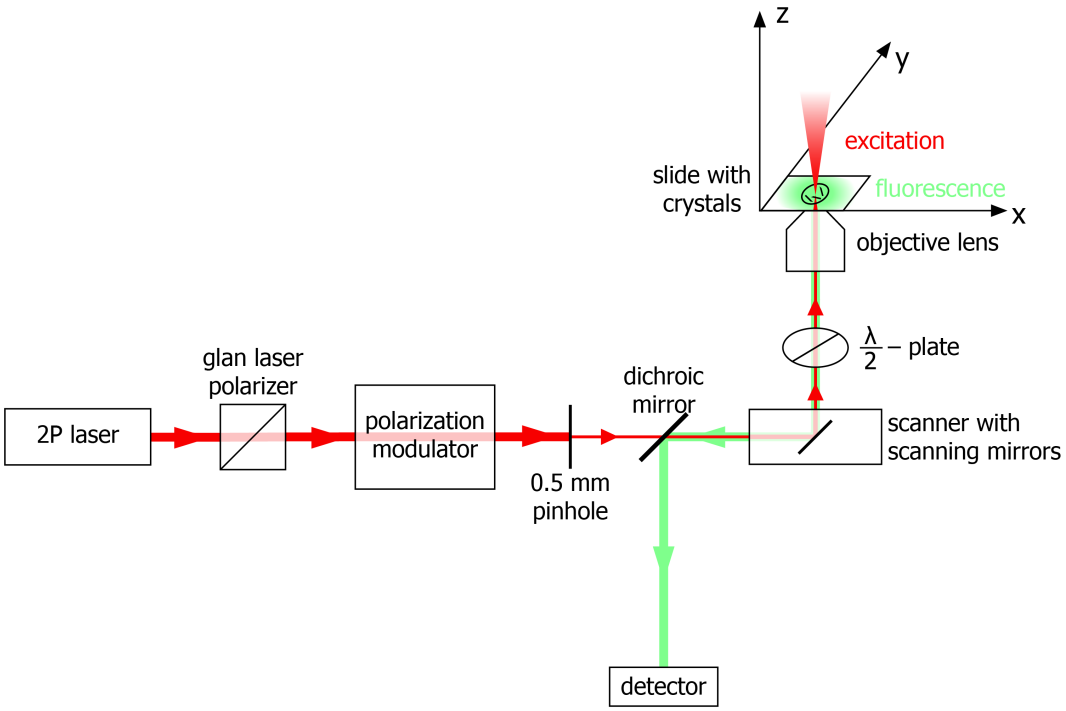

Figure 2.5: 2P polarization microscopy setup. Note that, in contrast to 1P setup, there is no confocal pinhole prior to the PMT detector.

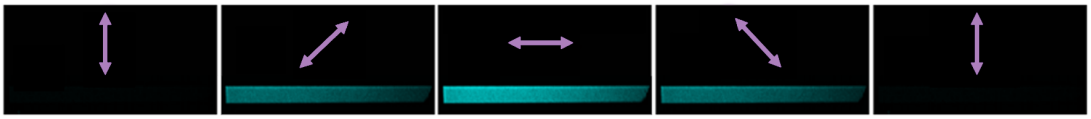

Figure 2.6: Illustration of a 1P polarization microscopy measurement of mTurquoise FP crystal. Here, only five snapshots are shown from the total of 73 images. Violet arrows show orientation of linear polarization of the excitation light ($\vec{e}$) in each snapshot. Here we observe maximum of fluorescence intensity for vector $\vec{e}$ oriented parallelly to the long axis of the crystal, and minimum – for $\vec{e}$ oriented perpendicularly to the long axis of the crystal.

An example of a 1P polarization microscopy measurement of a FP crystal (mTurquoise in this case) is shown at the Figure 2.6. As the linear polarization of the excitation light ($\vec{e}$) was rotated in the plane of the crystal (xy), the rate of crystal's fluorescence would change. As expected (since function $\cos^2 \alpha$ has a period π), the observed change in fluorescence was periodical with a period π.

By processing acquired raw image series (for different orientations of the polarization of excitation light with respect to the crystal) in the ImageJ software, namely subtracting background signal and averaging fluorescence values over a selected area of the crystal, we would get experimental dependence of fluorescence intensity on the angle α in between vector $\vec{e}$ and a long axis of the crystal (see Figure 3.2).

2.4 Quantum mechanical calculations

In this thesis, we hypothesize that 2P absorptivity tensors of studied representative FPs exhibit vector-like behaviour. In order to test this hypothesis, we chose to calculate 2P absorptivity tensors for the optimized fluorophore structures in vacuum. That was done in several consequent steps.

First, using published structures of fluorophores of FPs of interest, we would manually build fluorophores ground-state geometries in MOLDEN software. Structures used for quantum mechanical (QM) calculations in this thesis are described in the Figure 1.5. Then, we would perform geometry optimization of these structures in Gaussian16 software package, using Hartree-Fock (and at times B3LYP) functional and 6-31G basis set. Coordinates of obtained optimised mTurquoise, eGFP and mCherry fluorophore structures are listed in tables A.6, A.7 and A.8 respectively. Finally, for each optimized fluorophore we would calculate 2PAT for the excitation from the ground electronic state to the first excited state in DALTON software package, using time-dependent density functional theory method with B3LYP functional and 6-31G basis set.

2.5 Mathematical modelling

In order to analyse our polarization microscopy measurements in terms of directional optical properties of individual FP molecules, we needed to bring together

two coordinate systems: a microscopic, PDB coordinate system, in which the coordinates of individual atoms age given, and a macroscopic, laboratory coordinate system, in which we perform polarization microscopy measurements. Knowledge of the orientation of crystallographic axes a, b, c within a crystal allows us to do that. As has been described earlier (see Figures 2.4 and 2.5), during polarization microscopy measurements the electric field vector $\vec{e}$ is rotating within the plane of the slide (xy). With the assumption that a measured FP crystal is sitting flat in the slide (see *Discussion*) that as well means that vector $\vec{e}$ rotates within the plane of the crystal (see Figure 2.7). Therefore, if we know orientations of crystallographic axes a, b, c with respect to the macroscopic environment, we know the orientation of electric field vector $\vec{e}$ with respect to crystallographic axes a, b, c.

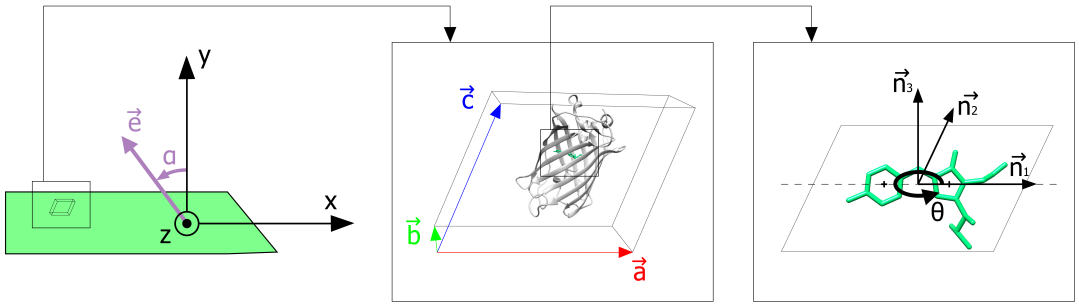

Figure 2.7: Coordinate systems used in mathematical modelling. Since in this thesis we work with relative orientations of linear polarization of excitation light (denoted by vector $\vec{e}$) and FP molecules, when defining coordinate systems we only need to define orientations of their axes, not positions of their origins. First, in our polarization microscopy measurements we work in a macroscopic, laboratory coordinate system xyz, defined as following: axis x is parallel to the long axis of the crystal, axis z is perpendicular to the plane in which the linear polarization of excitation light ($\vec{e}$) is rotated (counter-clockwise around z axis by angle α) and axis y is perpendicular to both x and z axes, making xyz a right-handed Cartesian coordinate system (left image). FPs structures are defined in crystallographic, PDB coordinate system. Axes defining crystallographic unit cell are labelled as a, b, and c in accordance with general convention (central image). Finally, since absorption properties of FPs are associated with their fluorophores, here we define a third coordinate system, $n_1n_2n_3$, associated with a FP's fluorophore (right image). Here, axis n_3 is a normal to the approximating plane of a fluorophore, axis n_1 is defined by the centres of two planar aromatic rings, and axis n_2 is perpendicular to both n_1 and n_3 axes, making $n_1n_2n_3$ a right-handed Cartesian coordinate system. Then, orientation of a vector of interest (a TDM for 1P absorption or a MARV for 2P absorption) within a FP molecule is given by angle θ, corresponding to the counter-clockwise rotation around the plane normal $\vec{n}_3$ from the centre line $\vec{n}_1$ (directions as shown at the right image).

Studied absorption properties of FPs are associated with their fluorophores. In this thesis, instead of working with 3D structures of fluorophores, we make an assumption (as it is made in Ansbacher et al. [2012]) that vectors $\vec{\mu}$ and $\vec{\mu}^{2P}$ lie within the approximating plane of the fluorophore's system of conjugated double

Table 2.2: Obtained parameters of mTurquoise, eGFP and mCherry approximating fluorophore planes. For each FP, a PDB file used for analysis, as well as centre line $\vec{n}_1$ and plane normal $\vec{n}_3$ coordinates within corresponding PDB coordinate systems are listed. Atoms selected for plane approximation are shown in Figure 1.5.

	mTurquoise	**eGFP**	**mCherry**
PDB	4AR7	2Y0G	2H5Q
$\vec{n}_1$	$\{-0.875, -0.401, 0.271\}$	$\{-0.883, -0.458, 0.103\}$	$\{0.831, -0.541, -0.131\}$
$\vec{n}_3$	$\{-0.450, 0.881, -0.145\}$	$\{-0.469, 0.864, -0.181\}$	$\{-0.509, -0.833, 0.214\}$

bonds (see Figure 2.7) for all FPs studied in this thesis. These approximating planes were obtained by fitting selected fluorophore's atoms PDB coordinates (see Figure 1.5) with a plane using least-square algorithm. Normals $\vec{n}_3$ defining obtained approximating planes and corresponding centre lines $\vec{n}_1$ (with directions as shown at the Figure 2.7) are listed in the Table 2.2 for each fluorophore. Therefore, we know orientations of axes $\vec{n}_1, \vec{n}_3$ with respect to crystallographic axes a, b, c, and orientations of a, b, c axes with resect to the electric field vector $\vec{e}$.

Once we have defined fluorophore's coordinate system $n_1n_2n_3$, and since we assume that vectors $\vec{\mu}$ (a TDM, describing anisotropy of 1P absorption) and $\vec{\mu}^{2P}$ (a MARV, describing anisotropy of 2P absorption in case of a single dominant eigenvalue of 2PAT) lie within the n_1n_2 plane, orientations of vectors $\vec{\mu}$ and $\vec{\mu}^{2P}$ within a FP molecule can be defined by $\vec{n}_1$, $\vec{n}_3$ coordinates (are known, listed in the Table 2.2) and an angle θ (more specifically, θ^{1P} for $\vec{\mu}$ and θ^{2P} for $\vec{\mu}^{2P}$), corresponding to the counter-clockwise rotation around the plane normal $\vec{n}_3$ from the line $\vec{n}_1$ connecting centres of two aromatic rings (centres are shown in the Figure 1.4).

In this work we study dependence of rate of absorption (1P or 2P) on relative orientation of the linear polarization of excitation light (denoted by vector $\vec{e}$) and a FP molecule. Therefore, in our calculations we can neglect translation transformation and only implement rotations. Rotations are introduced by multiplication of a geometric object of interest (for example, a vector) by an according rotation matrix. For example, to rotate vector $\vec{e}$ in the xy plane around z axis by angle α (where $\alpha > 0$ for counter-clockwise rotation), we need to multiply vector $\vec{e}$ by a rotation matrix $R(\alpha)$:

$$R(\alpha) \cdot \vec{e} = \begin{pmatrix} \cos\alpha & -\sin\alpha & 0 \\ \sin\alpha & \cos\alpha & 0 \\ 0 & 0 & 1 \end{pmatrix} \cdot \vec{e}. \tag{2.1}$$

All mathematical modelling and data fitting described in this thesis was done in Wolfram Mathematica software. To implement necessary rotations, a built-in function, *RotationMatrix*, was used (see *Examples of Wolfram Mathematica code*).

Now that we can bring together two coordinate systems – the one in which we rotate the electric field vector $\vec{e}$ by angle α, the laboratory coordinate system (xyz), and the one in which we define TDM and MARV (by angles $\theta^{1P}$and θ^{2P} respectively), the fluorophore's coordinate system $(n_1n_2n_3)$ – we can calculate

the rate of absorption by a single crystallographic unit cell of FP crystal. Note that here we work with normalized vectors $\vec{\mu}$ and $\vec{\mu}^{2P}$ and assume that they are in units of length for the sake of geometrical considerations. For the rate of 1P absorption we get:

$$R^{1\mathrm{P}}(\alpha;\theta^{1\mathrm{P}}) \sim \sum_{i=1}^{N}(\vec{e}\cdot\vec{\mu_i})^2, \tag{2.2}$$

where N is a number of symmetry operations for a crystallographic unit cell and $\vec{\mu_i}$ is obtained by applying i-th symmetry operation to the TDM $\vec{\mu}$ (see Table 3.2).

Similarly, in case of 2P absorption by a FP molecule, which 2PAT has a single dominant eigenvalue (with a corresponding MARV $\vec{\mu}^{2\mathrm{P}}$), the rate of absorption can be calculated as:

$$R^{2\mathrm{P}}(\alpha;\theta^{2\mathrm{P}}) \sim \sum_{i=1}^{N}(\vec{e}\cdot\vec{\mu_i}^{2\mathrm{P}})^4. \tag{2.3}$$

Since in our polarization microscopy experiments we control linear polarization of the excitation light while collecting all fluorescent signal, the rate of observed fluorescence is proportional to the rate of absorbance and hence is representative of anisotropy of light absorption by a FP molecule. Therefore, we can use Equations 2.2 and 2.3 to calculate a rate of fluorescence for a single crystallographic unit cell of FP crystal for 1P and 2P excitations respectively:

$$F^{1\mathrm{P}}(\alpha;\theta^{1\mathrm{P}}) \sim \sum_{i=1}^{N}(\vec{e}\cdot\vec{\mu_i})^2, \tag{2.4}$$

$$F^{2\mathrm{P}}(\alpha;\theta^{2\mathrm{P}}) \sim \sum_{i=1}^{N}(\vec{e}\cdot\vec{\mu_i}^{2\mathrm{P}})^4. \tag{2.5}$$

Using these equations, we can predict what a ratio r of fluorescence obtained with the polarization of the incident light parallel to the long axis of the crystal F_x^{1P} to the fluorescence obtained with the polarization of the incident light perpendicular to the long axis of the crystal F_y^{1P} would be for 1P absorption:

$$r^{1\mathrm{P}}(\theta^{1\mathrm{P}}) = \frac{F_x^{1P}}{F_y^{1P}} = \frac{\sum_{i=1}^{N}(\vec{e}_x\cdot\vec{\mu_i})^2}{\sum_{i=1}^{N}(\vec{e}_y\cdot\vec{\mu_i})^2}, \tag{2.6}$$

where $\vec{e}_x = \{1,0,0\}$ and $\vec{e}_y = \{0,1,0\}$. Similarly we define a ratio r^{2P} for 2P absorption in case of a single dominant eigenvalue of 2PAT:

$$r^{2\mathrm{P}}(\theta^{2\mathrm{P}}) = \frac{F_x^{2P}}{F_y^{2P}} = \frac{\sum_{i=1}^{N}(\vec{e}_x\cdot\vec{\mu_i}^{2\mathrm{P}})^4}{\sum_{i=1}^{N}(\vec{e}_y\cdot\vec{\mu_i}^{2\mathrm{P}})^4}. \tag{2.7}$$

Note that ratios r^{1P}, r^{2P} no longer depend on the orientation of electric field vector $\vec{e}$ (defined by angle α) but only on the orientation of a TDM ($\vec{\mu}$, defined by angle $\theta^{1\mathrm{P}}$), and MARV ($\vec{\mu}^{2P}$, defined by angle $\theta^{2\mathrm{P}}$), respectively. Also, ratios r^{1P} and r^{2P}, calculated for a singe unit cell, stay the same for a monocrystalline structure. In this thesis, we will use these ratios – along with the assumption of a vector-like behaviour of 2P absorption by a FP molecule – to analyse our polarization microscopy measurements in terms of TDM ($\vec{\mu}$) and MARV ($\vec{\mu}^{2P}$) orientations.

3. Results

3.1 Structural and orientational information on FPs crystals

After several rounds of crystallization we have obtained crystals of three studied FPs. Crystals were then subjected to X-ray diffraction measurements for the sake of structural analysis. Space groups of examined crystals have been determined. Our experiments showed that under the chosen crystallization conditions FPs largely formed crystals of only one crystallographic group. Pictures of representative FP crystals, orientations of crystallographic axes with respect to the crystals and schematic representations of crystallographic unit cells are shown in the Figure 3.1. Detailed information on FPs crystals space groups is listed in tables 3.1 and 3.2.

FPs of eGFP and mTurquoise have crystallized into P212121 (orthorhombic) space group. Obtained structures corresponded to 2Y0G (eGFP) and 4AR7 (mTurquoise2) structures listed at the Protein Data Bank (PDB). For eGFP and mTurquoise crystals axes of the crystallographic unit cell were assumed to coincide with macroscopic symmetry axes of the crystal, with a axis oriented parallel to the long axis of the crystal, b axis lying in the plane of the crystal perpendicular to the a axis and axis c being perpendicular to the plane of the crystal (according to Rosell and Boxer [2003]) (see Figure 3.1-a,b).

FP of mCherry has crystallized into P21 (monoclinic) space group. Structure obtained corresponded to the 2H5Q structure listed at the PDB. Our analysis of X-ray diffraction measurements have shown that in mCherry crystals crystallographic axis a coincides with the long axis of the crystal and axis b lies in the plane of the crystal perpendicularly to a (see Figure 3.1-c).

Table 3.1: Quantitative information on crystallographic space groups. For each FP a corresponding space group, number of symmetries in the space group, lengths of unit cell edges (a, b, c, in angstroms) and the angles between them (α, β, γ) are listed.

	mTurquoise	**eGFP**	**mCherry**
Space group	P212121	P212121	P21
Number of symmetries N	4	4	2
a, Å	51.5	51	49
b, Å	62.5	62.0	43
c, Å	69.5	70.0	61
α, °	90	90	90
β, °	90	90	112
γ, °	90	90	90

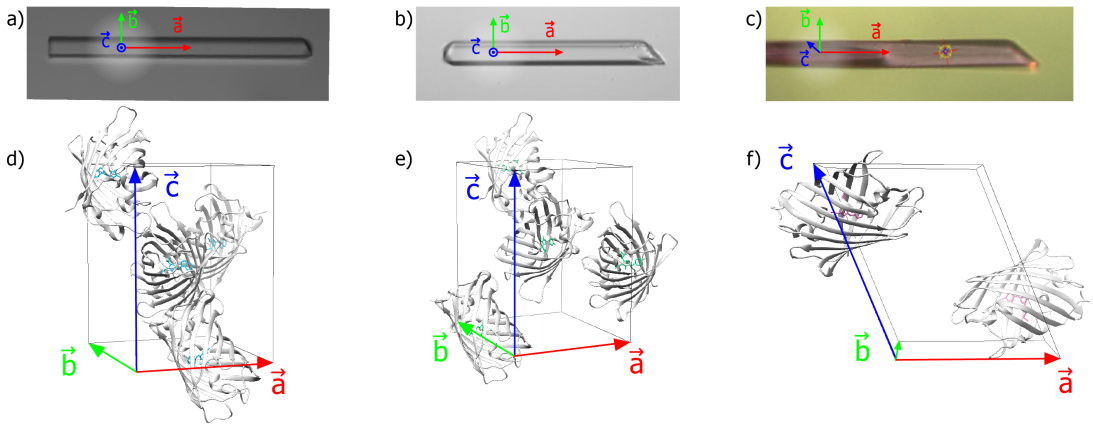

Figure 3.1: Structural and orientational information on obtained FPs crystals. a), b), c) Pictures of mTurquoise, eGFP and mCherry crystals respectively. Crystallographic axes a, b and c are coloured in red, green and blue according to the standard convention. Here we can see, that for all FPs crystals axis a coincides with the long axis of the crystal, and both a and b axes lie in the plane of the crystal. d), e), f) Pictures of mTurquoise, eGFP and mCherry crystallographic unit cells. For crystals of mTurquoise and eGFP, unit cell consists of four FP molecules (hence has four unique TMD/MARV orientations; $N = 4$). mCherry FP crystal unit cell has two FP molecules (hence two unique TMD/MARV orientations; $N = 2$).

Table 3.2: List of space group symmetry operations. Here we can see that there are four symmetry operations for P212121 space group and two symmetry operations for P21 space group. For example, $\{-1, 1, -1\}$ symmetry operation means that if we have an atom with $\{x, y, z\}$ coordinates in PDB file ($\{1, 1, 1\}$ symmetry operation), in a single unit cell there will another atom of the same type with coordinates $\{-x, y, -z\}$. We use this information to calculate ratios r^{1P} and r^{2P} (see Equations 2.6 and 2.7).

P212121 $N = 4$	**P21** $N = 2$
$\{1, 1, 1\}$	$\{1, 1, 1\}$
$\{-1, 1, -1\}$	$\{-1, 1, -1\}$
$\{-1, -1, 1\}$	
$\{1, -1, -1\}$	

3.2 Polarization microscopy measurements on FPs crystals

3.2.1 One-photon polarization microscopy

In our 1P polarization microscopy experiments we have observed the change of FP crystal fluorescence with rotation of the electric field vector $\vec{e}$ within the plane of the crystal (see Figure 2.6). By processing raw image series (acquired at different orientations of electric field vector $\vec{e}$ with respect to the crystal) in the ImageJ software, we have obtained experimental dependence of FP crystal fluorescence on the orientation of linear polarization of excitation light $\vec{e}$ (given by angle α) (see Figure 3.2). For all measured FPs crystals the maximum of fluorescence was observed when vector $\vec{e}$ was parallel to the long axis of the crystal (axis x).

Then, experimental curves have been fitted using least-square algorithm. For obtained approximating functions $F^{1P}_{exp}(\alpha)$ we have calculated the ratio r^{1P}_{exp} (in analogy with Equation 2.6) for each individual crystal:

$$r^{1P}_{exp} = \frac{(F^{1P}_{exp})_x}{(F^{1P}_{exp})_y} = \frac{F^{1P}_{exp}(90°)}{F^{1P}_{exp}(0°)}. \tag{3.1}$$

Values of r^{1P}_{exp} obtained for individual crystals and parameters of the fitting are listed in the Tables A.1 (A.2), A.3 and A.4 for mTurquoise, eGFP and mCherry FPs respectively. Then, an arithmetic mean value $\overline{r^{1P}_{exp}}$ was calculated for each FP (see Table 3.3). These values will be used for further analysis of experimental data in terms of TDM orientations in studied FPs.

Table 3.3: Values of $\overline{r^{1P}_{exp}}$ for studied FPs. For each type of FP crystals, a number of measured crystals (n), according acquisition wavelength (λ) and an arithmetic mean value $\overline{r^{1P}_{exp}}$ with its standard deviation (σ) are listed. For further analysis (in terms of TDM orientations in studied FPs), the mTurqioise *mixed* 488 nm, eGFP 405 nm and mCherry 515 nm $\overline{r^{1P}_{exp}}$ values have been used (for the reasoning behind this choice see *Uneven light penetration*).

FP crystals	**n**	**λ, nm**	$\overline{\boldsymbol{r^{1P}_{exp}}} \pm \boldsymbol{\sigma}$
mTurquoise	38	405	2.69 ± 0.65
	38	488	5.62 ± 0.55
mTurquoise *mixed*	24	405	5.20 ± 0.28
	24	488	5.13 ± 0.18
eGFP	42	405	3.69 ± 0.87
	41	488	1.83 ± 0.49
mCherry	8	515	1.43 ± 0.32

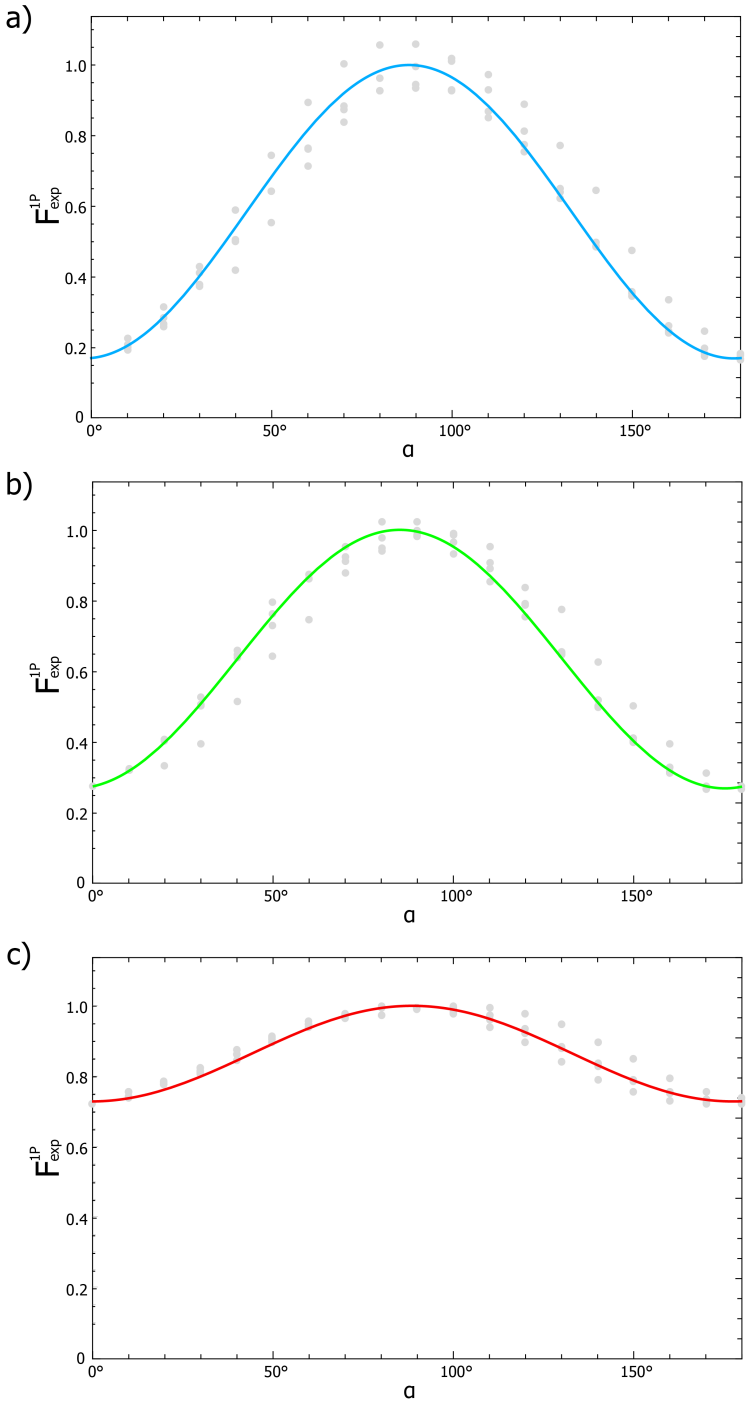

Figure 3.2: a), b), c) Examples of experimental curves obtained from 1P polarization microscopy measurements on mTurquoise, eGFP and mCherry FPs crystals respectively. Each image corresponds to a single crystal measurement. Grey dots represent experimentally acquired values of fluorescence at different orientations of linear polarization of excitation light $\vec{e}$ (with 10° step over the 0÷720° range). Solid lines correspond to approximating functions $F^{1P}_{exp}(\alpha)$ used for calculation of ratios r^{1P}_{exp}. Experimental data and fitting curves are plotted over the 0÷180° range since the rate of fluorescence is periodical with period π. $\alpha = 0°$ for vector $\vec{e}$ perpendicular to the long axis of the crystal (axis x), $\alpha = 90°$ – for vector $\vec{e}$ parallel to x. Fluorescence intensities are normalized to $max\{F^{1P}_{exp}(\alpha)\} = 1$.

3.2.2 Two-photon polarization microscopy

Similar measurements have been performed on FPs crystals with 2P excitation. For all measured mTurquoise and eGFP FPs crystals the maximum of fluorescence was observed for the linear polarization of excitation light (denoted by vector $\vec{e}$) parallel to the long axis of the crystal (axis x), similar to what we have observed in 1P polarization microscopy measurements. For measured mCherry FP crystal dependence of fluorescence intensity on the linear polarization of the 2P excitation light had a different profile than that for 1P excitation (see Figure 3.3).

Then, experimental curves have been fitted using least-square algorithm. For obtained approximating functions $F^{2P}_{exp}(\alpha)$ we have calculated the ratio r^{2P}_{exp} (in analogy with Equation 2.7) for each individual crystal:

$$r^{2P}_{exp} = \frac{(F^{2P}_{exp})_x}{(F^{2P}_{exp})_y} = \frac{F^{2P}_{exp}(90^\circ)}{F^{2P}_{exp}(0^\circ)}. \tag{3.2}$$

Values of r^{2P}_{exp} obtained for individual crystals and parameters of the fitting are listed in the Table A.5 for all studied FPs. Then, an arithmetic mean value $\overline{r^{2P}_{exp}}$ was calculated for each FP (see Table 3.4). These values will be used for further analysis of experimental data in terms of MARV orientations in studied FPs.

Table 3.4: Values of $\overline{r^{2P}_{exp}}$ for studied FPs. For each type of FP crystals, a number of measured crystals (n), according acquisition wavelength (λ) and an arithmetic mean value $\overline{r^{2P}_{exp}}$ with its standard deviation (σ) are listed. Note that there is only a single mCherry crystal measured with 2P excitation.

FP crystals	**n**	**λ, nm**	$\boldsymbol{\overline{r^{2P}_{exp}} \pm \sigma}$
mTurquoise	13	810	21.76 ± 5.74
eGFP	6	810	16.51 ± 9.03
mCherry	1	960	1.76

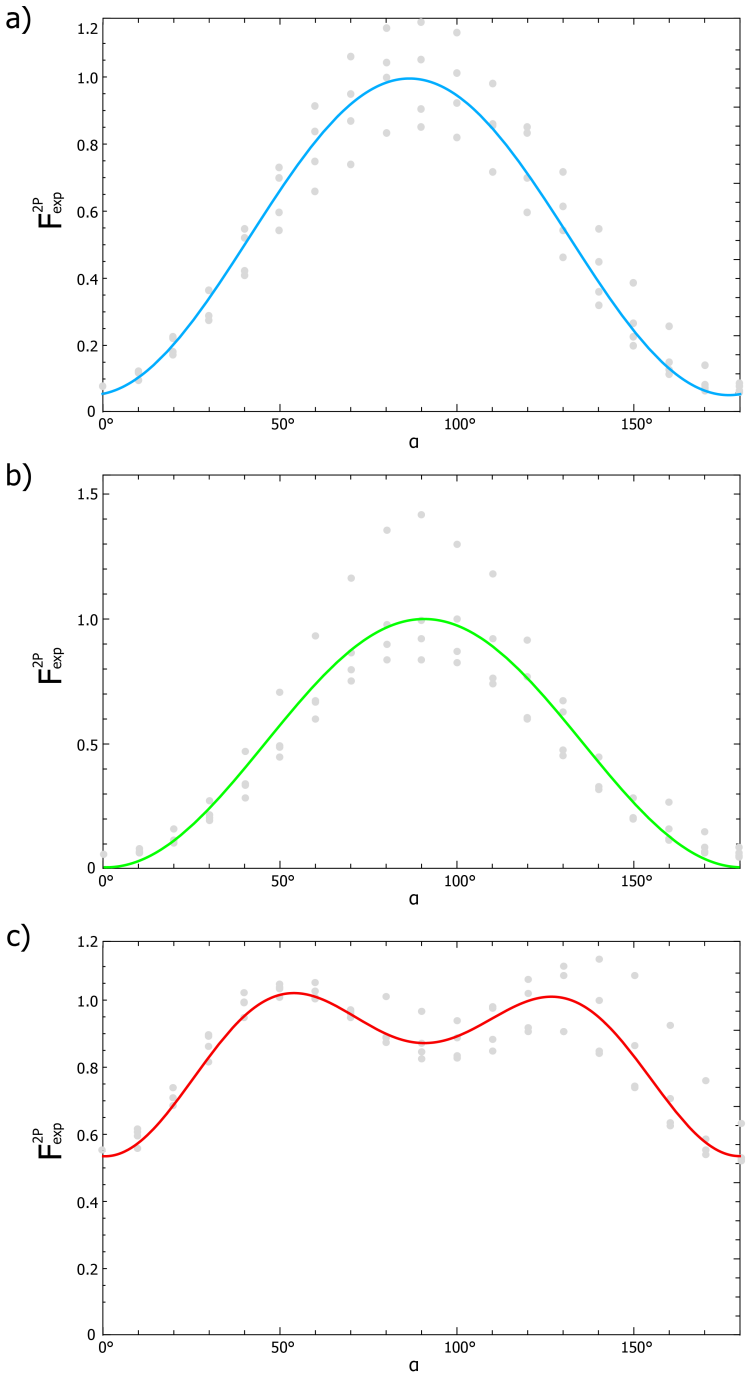

Figure 3.3: a), b), c) Examples of experimental curves obtained from 2P polarization microscopy measurements on mTurquoise, eGFP and mCherry FPs crystals respectively. Each image corresponds to a single crystal measurement. Grey dots represent experimentally acquired values of fluorescence at different orientations of linear polarization of excitation light $\vec{e}$ (with 10° step over the 0÷720° range). Solid lines correspond to approximating functions $F^{2P}_{exp}(\alpha)$ used for calculation of ratios r^{2P}_{exp}. Experimental data and fitting curves are plotted over the 0÷180° range since the rate of fluorescence is periodical with period π. $\alpha = 0°$ for vector $\vec{e}$ perpendicular to the long axis of the crystal (axis x), $\alpha = 90°$ – for vector $\vec{e}$ parallel to x. Fluorescence intensities are normalized to $max\{F^{2P}_{exp}(\alpha)\} = 1$.

3.3 Analysis of experimental data in terms of TDM orientations

Once we have obtained structural information on FPs crystals and established the orientations of crystallographic unit cells with respect to the crystals (see *Structural and orientational information on FPs crystals*), we moved on to the analysis of our experimental data in terms of TDM orientations in studied FPs.

Theoretical dependencies of the ratio r^{1P} on the possible orientation of TDM ($\vec{\mu}$) within the approximating plane of a fluorophore (defined by angle θ^{1P}) in studied FPs were calculated by rotating vector $\vec{\mu}$ around the plane's normal $\vec{n_3}$ by angle θ^{1P} from the centreline $\vec{n_1}$ (see Figure 2.7 and Table 2.2) and using Equation 2.6 (for further details, see *Examples of Wolfram Mathematica code*). Obtained theoretical curves $r^{1P}(\theta^{1P})$ are given in the Figure 3.4 for the three studied FPs.

Comparison of these theoretical dependencies $r^{1P}(\theta^{1P})$ with experimentally determined $\overline{r_{exp}^{1P}}$ values (see Table 3.3) gives us two possible TDM orientations, θ_1^{1P} and θ_2^{1P}, for each FP (see Figure 3.4). These orientations are listed in the Table 3.5 along with the orientations obtained by means of QM calculations in Ansbacher et al. [2012]. We see that our experimentally obtained θ_1^{1P} values differ from QM predictions by 8.2°, 11.3° and 7.0° for mTurquoise, eGFP and mCherry FPs respectively.

Table 3.5: Possible TDM orientations in studied FPs. For each FP, possible TDM orientations, θ_1^{1P} and θ_2^{1P}, are given for $\overline{r_{exp}^{1P}}$, $\overline{r_{exp}^{1P}} \pm \sigma$ (68% confidence interval) and $\overline{r_{exp}^{1P}} \pm 2\sigma$ (95% confidence interval) values. In the fourth column QM predictions for TDM orientations described in Ansbacher et al. [2012] are listed.

FP	$\boldsymbol{r_{exp}^{1P}}$	$\boldsymbol{\theta_1^{1P}}$, °	**QM**, °	$\boldsymbol{\theta_2^{1P}}$, °
mTurquoise	5.13	5.0	176.8	67.4
	5.13 + 0.18	7.2		67.3
	5.13 – 0.18	2.7		67.5
	5.13 + 2·0.18	9.2		67.2
	5.13 – 2·0.18	0.2		67.5
eGFP	3.69	179.5	10.8	77.0
	3.69 + 0.87	12.2		76.4
	3.69 – 0.87	161.6		77.8
	3.69 + 2·0.87	21.0		75.9
	3.69 – 2·0.87	139.4		79.0
mCherry	1.43	152.8	159.8	93.6
	1.43 + 0.32	162.8		93.0
	1.43 – 0.32	142.6		94.4
	1.43 + 2·0.32	172.2		92.4
	1.43 – 2·0.32	132.8		95.5

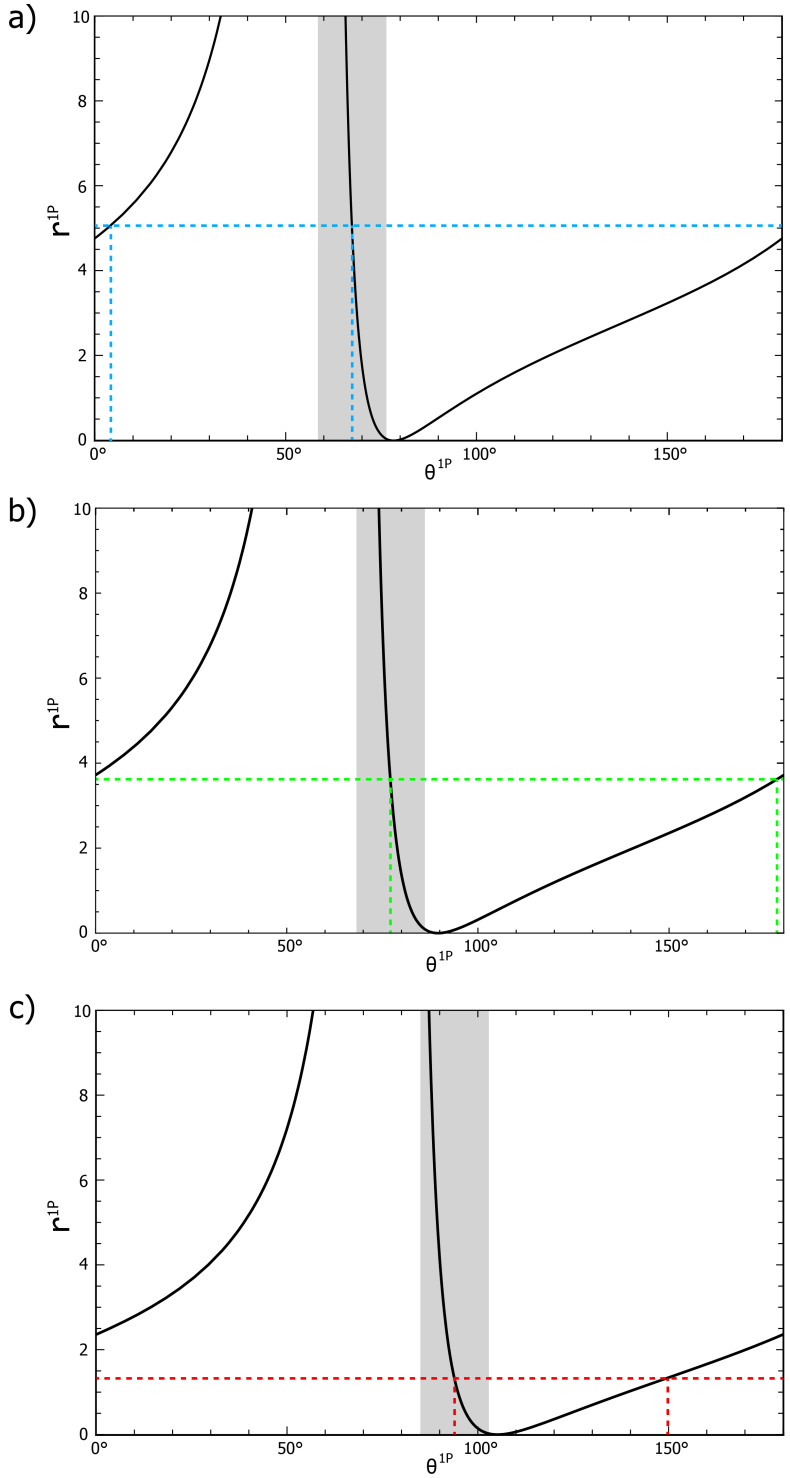

Figure 3.4: Possible TDM orientations in studied FPs. a), b), c) Calculated theoretical $r^{1P}(\theta^{1P})$ curves for mTurquoise, eGFP and mCherry FPs crystals respectively (solid black lines). An intercept of a theoretical curve with a horizontal line corresponding to the experimentally determined $\overline{r_{exp}^{1P}}$ value (coloured dashed lines) gives two possible TDM orientations, θ_1^{1P} and θ_2^{1P}, for each FP. Grey shaded areas highlight regions of rapid change of ratio r^{1P}. TDM orientations obtained in these regions are labelled θ_2^{1P} in the Table 3.5.

3.3.1 Uneven light penetration

As can be seen from the Table 3.3, our 1P polarization microscopy experiments on mTurquoise FP and eGFP crystals performed at different excitation wavelengths yielded inconsistent results in terms of $\overline{r_{exp}^{1P}}$ value.

Closer examination of our polarization microscopy imaging data revealed that the depth of penetration of linearly polarized excitation light into the FP crystal depends on the orientation of polarization of excitation light (denoted by vector $\vec{e}$) (see Figure 3.5). This in turn causes ratio r_{exp}^{1P} (see Equation 3.1) to change significantly along the depth of the crystal (see Figure 3.6).

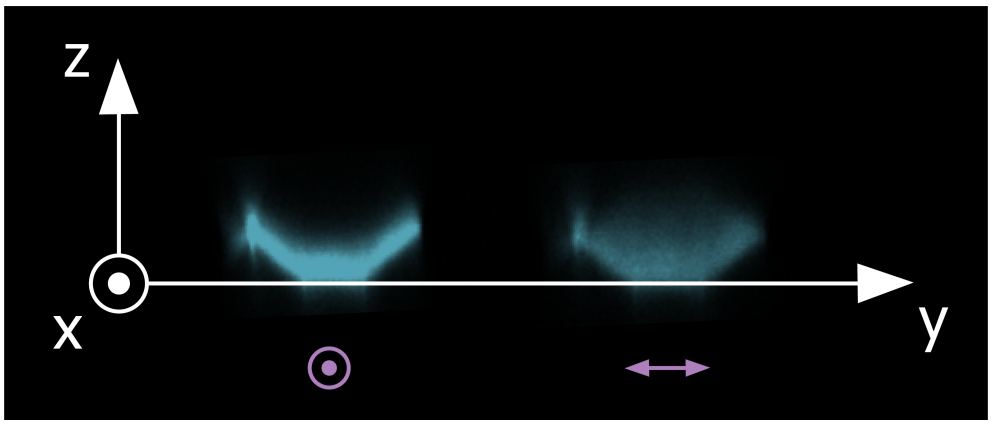

Figure 3.5: Two z-stack measurements of a thick (c. 20 µm) mTurquoise FP crystal acquired at 405 nm excitation wavelength with electric field vector $\vec{e}$ (violet symbols) oriented parallelly (left) and perpendicularly (right) to the long axis of the crystal (axis x). We can see that light polarized parallelly to the long axis of the crystal ($\alpha = 90°$) gets absorbed in the very first layers of the crystal, while light polarized perpendicularly to the long axis of the crystal ($\alpha = 0°$) penetrates deeper within the crystal.

Theoretical equation for the observed dependence of the ratio r_{exp}^{1P} on the depth of acquisition d within the FP crystal can be derived in the following way. Note that following equations are derived for a single crystallographic unit cell of FP crystal for the 1P excitation. According to the Lambert-Beer law,

$$\frac{I}{I_0} = 10^{-\varepsilon C d}, \tag{3.3}$$

where $I_0 = konst$ is the intensity of the incident light at the very bottom layer of the crystal ($d = 0$), I is the intensity of light at the depth d, C is the concentration of the attenuating species (i.e. fluorophore concentration) and ε is the molar attenuation coefficient.

In contrast to a solution of FP, where all FP molecule orientations are equally probable and the molar attenuation coefficient ε_{sol} is isotropic (i.e. the same in all directions), in FP crystal the molar attenuation coefficient ε_{cryst} is generally anisotropic. If we label a molar attenuation coefficient for a particular FP molecule, hence a particular TDM ($\vec{\mu}$) orientation, as ε_μ, then:

$$\varepsilon_{\text{sol}} = 2 \cdot \frac{\int \varepsilon_\mu \cdot (\vec{e} \cdot \vec{\mu})^2 \mathrm{d}\Omega}{\int \mathrm{d}\Omega} = 2 \cdot \frac{\varepsilon_\mu}{3} \Longrightarrow \varepsilon_\mu = \frac{3}{2}\varepsilon_{\text{sol}}, \tag{3.4}$$

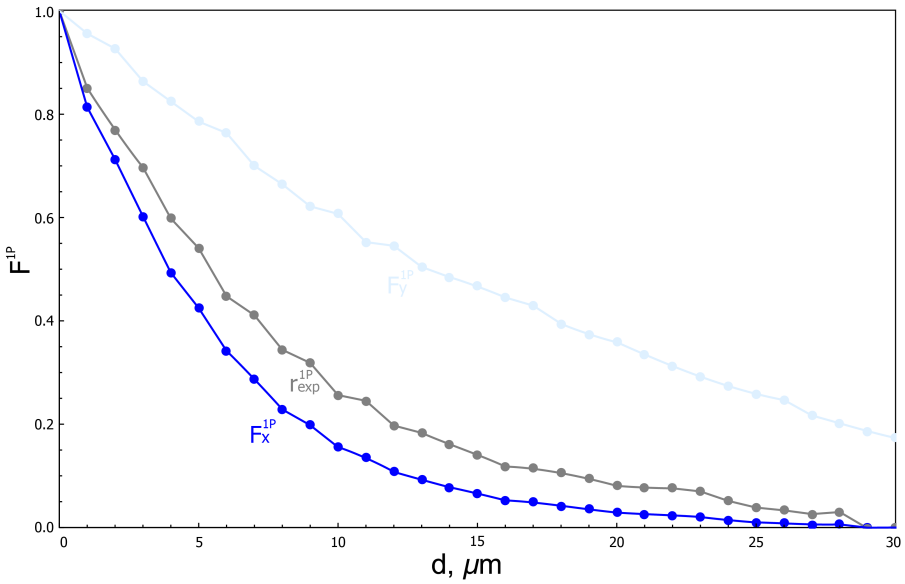

Figure 3.6: Experimental dependence of fluorescence intensities on the depth of acquisition (d) for the mTurquoise FP crystal shown at the Figure 3.5. We can see that fluorescence intensity for the excitation light polarized parallelly to the long axis of the crystal, F_x^{1P} (in deep blue), decays more rapidly than the fluorescence intensity for the excitation light polarized perpendicularly to the long axis of the crystal, F_y^{1P} (in light blue). Ratio of these two intensities, r_{exp}^{1P} (in grey), changes with the acquisition depth d. Starting point $d = 03$ corresponds to the very bottom layer of the crystal. Note that fluorescence intensities are normalized to $F_x^{1P}(0) = F_y^{1P}(0) = 1$ in order to emphasize polarization-dependent depth of the excitation light penetration, i.e. a constant is omitted in the plotted r_{exp}^{1P} dependence on d.

and ε_{cryst} can be calculated as:

$$\varepsilon_{\text{cryst}}(\alpha, \theta^{1P}) = \frac{1}{N}\sum_{i=1}^{N} \varepsilon_{\mu} \cdot (\vec{e} \cdot \vec{\mu_i})^2 = \frac{3}{2}\varepsilon_{\text{sol}} \cdot \frac{1}{N}\sum_{i=1}^{N} (\vec{e} \cdot \vec{\mu_i})^2, \tag{3.5}$$

where, as before, N is a number of symmetry operations for a crystallographic unit cell and $\vec{\mu_i}$ is obtained by applying i-th symmetry operation to the TDM $\vec{\mu}$ (see Table 3.2). Therefore, molar attenuation coefficients of a FP crystal for the excitation light linearly polarized along axes x and y, ε_{x} and ε_{y} respectively, can be calculated as:

$$\varepsilon_{\text{x}}(\theta^{1P}) = \frac{3}{2}\varepsilon_{\text{sol}} \cdot \frac{1}{N}\sum_{i=1}^{N} (\vec{e_x} \cdot \vec{\mu_i})^2, \tag{3.6}$$

$$\varepsilon_{\text{y}}(\theta^{1P}) = \frac{3}{2}\varepsilon_{\text{sol}} \cdot \frac{1}{N}\sum_{i=1}^{N} (\vec{e_y} \cdot \vec{\mu_i})^2, \tag{3.7}$$

where $\vec{e}_x = \{1, 0, 0\}$ and $\vec{e}_y = \{0, 1, 0\}$. Value of ε_{sol} for the mTurquoise FP is given at the Figure 1.4. Then, intensities of linearly polarized excitation light at the depth d of a FP crystal for the polarization parallel (I_x) and perpendicular (I_y) to the long axis of the crystal are:

$$I_x(d, \theta^{1P}) = I_0 \cdot 10^{-\varepsilon_x C d}, \tag{3.8}$$

$$I_y(d, \theta^{1P}) = I_0 \cdot 10^{-\varepsilon_y C d}. \tag{3.9}$$

Fluorophore concentration C for a single unit cell is calculated as:

$$C = \frac{\frac{N}{N_A}}{V}, \tag{3.10}$$

where N_A is the Avogadro's constant, and volume $V = abc$ (a, b, c are lengths of unit cell edges, see Table 3.1). Since in our polarization microscopy experiments we control linear polarization of the excitation light while collecting all fluorescent signal, the rate of observed fluorescence is proportional to the rate of absorbance and hence to the intensity of excitation light:

$$\frac{F_x^{1P}}{F_y^{1P}} \sim \frac{I_x}{I_y}. \tag{3.11}$$

Therefore, dependence of the ratio r_{exp}^{1P} (defined in the Equation 2.6) on the depth of acquisition d within the FP crystal can be calculated as:

$$r^{1P}(d, \theta^{1P}) = 10^{-(\varepsilon_x - \varepsilon_y) C d}. \tag{3.12}$$

This curve, calculated for a mTurquoise FP crystal in P212121 space group using $\theta^{1P} = QM$ is compared to the experimentally observed dependence at the Figure 3.7. Consistence of our experimental and calculation results gives us certainty in the Equation 3.12.

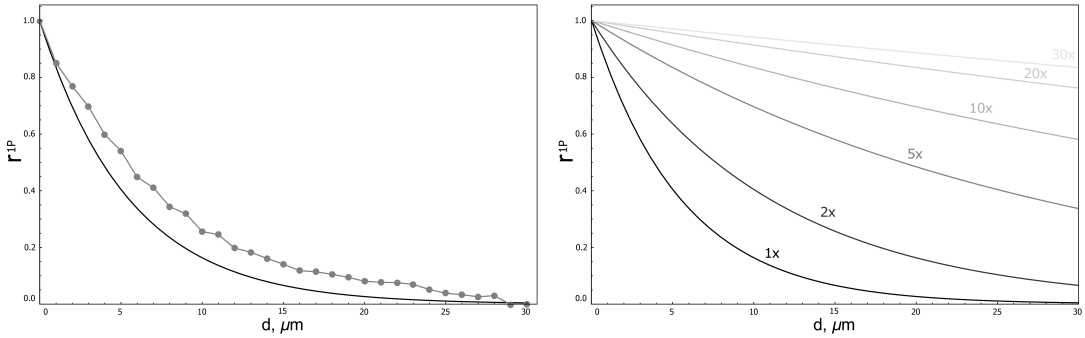

Figure 3.7: Left graph shows normalized dependencies of experimentally determined r_{exp}^{1P} (grey line with dots) and calculated r^{1P} (solid black line) (see Equation 3.12) values on the acquisition depth d for mTurquoise FP crystal in P212121 space group. Right graph shows $r^{1P}(d)$ curves calculated for the actual (*1x*) FP fluorophore concentration (see Equation 3.10) as well as for several concentration dilutions ($2x$, $5x$, $10x$, $20x$, $30x$). It follows from the right graph that a $20x$ dilution of fluorophore concentration in a crystal would result in almost constant value of r^{1P} within the typical acquisition range (c. $0 \div 10\,\mu m$).

Therefore, we have confirmed that ratio r^{1P} depends on the depth of acquisition d within the FP crystal. Since, due to technical limitations of our polarization

microscopy measurements, we cannot precisely control the depth of acquisition within measured FP crystals, we need the ratio r^{1P} to stay close to constant within the acquisition range in order for the values of $\overline{r_{exp}^{1P}}$ obtained at different excitation wavelengths to be consistent. First derivative of the Equation 3.12 suggests that it can be achieved by decreasing fluorophore concentration C within FP crystals (see Figure 3.7):

$$\frac{\mathrm{d}(r^{1P})}{\mathrm{d}d} = -(\varepsilon_x - \varepsilon_y)C \cdot 10^{-(\varepsilon_x - \varepsilon_y)Cd}. \tag{3.13}$$

In the course if this work, we have managed to obtain mTurquoise FP crystals with decreased fluorophore concentration by co-crystallizing FP of mTurquoise with its non-fluorescent variant mTurquoiseW67A (see Figure 3.8). Resulting crystals of mTurquoise FP with decreased fluorophore concentration are referred to in this thesis as *mixed* crystals. Plasmid encoding desired mutant gene was prepared by the PCR with suitable phosphorylated primers followed by ligation. We have noticed that these two proteins would co-crystallize better if they were lysed/purified together, rather than if they were manually mixed in a crystallization drop. Therefore, cell cultures containing FP of mTurquoise and its non-fluorescent variant, mTurquoiseW67A, mixed in a desired proportion (c. 1 : 20), were fist co-purified by affinity chromatography on a nickel column and then co-crystallized using standard procedures and conditions described in this thesis (see *Protein purification and crystallisation*). For further detail, see *Non-fluorescent mutant of mTurquoise FP*.

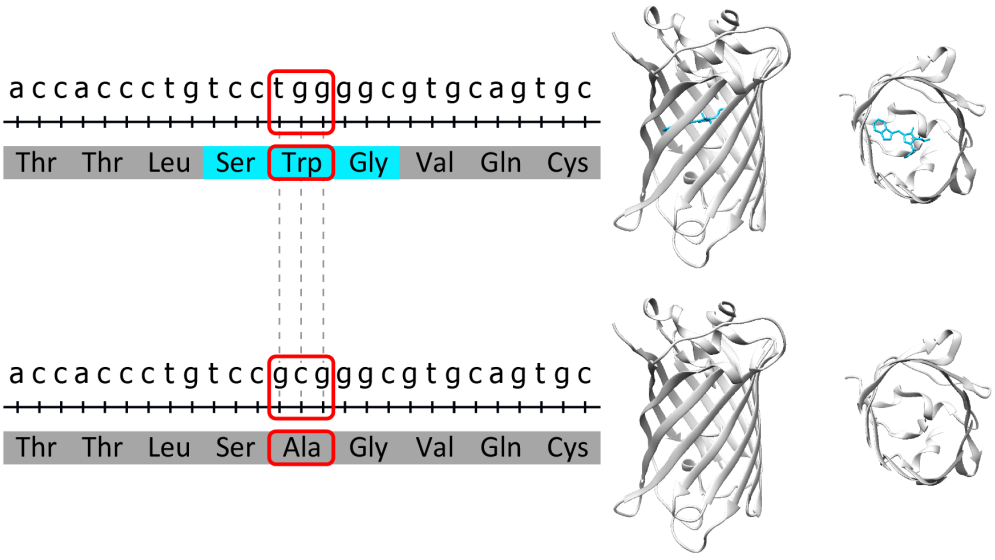

Figure 3.8: Non-fluorescent mutant of mTurquoise FP, mTurquoiseW67A, carries a single amino acid mutation in the three amino acids (Ser-Trp-Gly) forming mTurquoise FP fluorophore (SWG). This mutation is introduced by the change of two nucleotides in the tryptophan codon at the 67th position, which leads to formation of a new amino acid, alanine, instead. Due to this mutation, SWG fluorophore no longer forms, and the resulting protein, mTurquoiseW67A, has the same β-barrel structure as the original fluorescent mTurquoise protein but does not exhibit fluorescence.

Values of ratio $\overline{r_{exp}^{1P}}$ obtained from 1P polarization microscopy measurements on *mixed* crystals at 405 nm and 488 nm excitation wavelengths are highly consistent (see Figure 3.9).

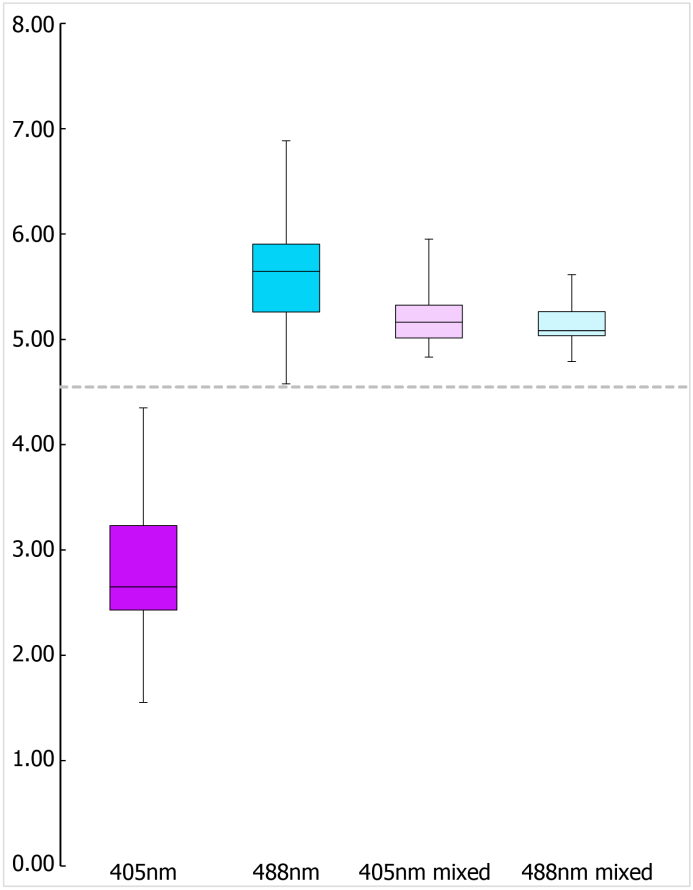

Figure 3.9: Box and whiskers plot comparing r_{exp}^{1P} values obtained for normal and *mixed* mTurquoise FP crystals at two excitation wavelengths, 405 nm (close to the maximum of the excitation spectrum) and 488 nm (close to te edge of the excitation spectrum). We can see that *mixed* mTurquoise FP crystals give comparable results at both excitation wavelengths; these results are also comparable with the results of the normal mTurquoise FP crystal measurements with 488 nm excitation wavelength.

As we move further away from the peak of the FP excitation spectrum, probability of absorption of an excitation light photon by a FP molecule decreases. Consistence of results of our measurements on *mixed* crystals at 405 nm and 488 nm excitation wavelengths with the results of the normal mTurquoise FP crystal measurements with 488 nm excitation wavelength (see Figure 3.9) suggests that imaging of FP crystals at the edge of the excitation spectrum is practically equivalent to reducing FP fluorophore concentration with FP crystals. Based on this assumption and due to the technical difficulty of purification and crystallization of *mixed* crystals, for mathematical analysis of experimental polarization microscopy data in terms of TDM orientations in eGFP and mCherry FPs we use $\overline{r_{exp}^{1P}}$ values acquired at 405 nm and 515 nm excitation wavelengths respectively (see Table 3.3).

3.3.2 Multiple solutions

Mathematical analysis of our 1P polarization microscopy data gives two possible TDM orientations, θ_1^{1P} and θ_2^{1P}, for each FP (see Figure 3.4). However, while both orientations correspond the same value of r^{1P}, their calculated fluorescence intensity profiles significantly differ in magnitude (see Figure 3.10).

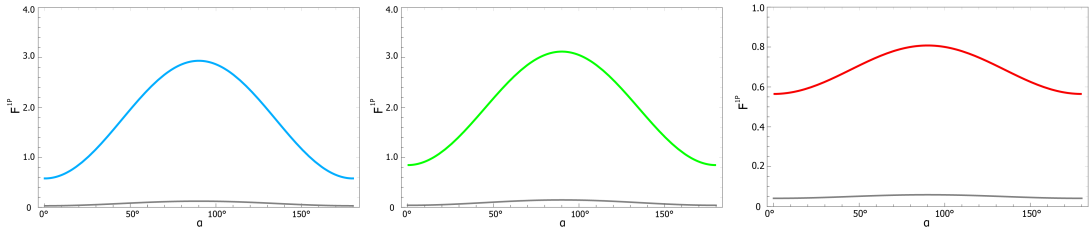

Figure 3.10: Calculated dependencies of fluoresce intensity for 1P excitation F^{1P} (see Equation 2.2) on the orientation of polarization of excitation light (given by angle α) in mTurquoise (left), eGFP (centre) and mCherry (right) FPs for two possible TDM orientations, θ_1^{1P} (coloured lines) and θ_2^{1P} (grey lines).

Also, as can be seen from the Figure 3.4, angle θ_2^{1P} corresponds to the area where r^{1P} rapidly changes with a slightest change of TDM orientation – a quality that we most probably would observe during our polarization microscopy measurements, as slight rotation of crystals around their long axes would then cause dramatic change of r_{exp}^{1P} value. Furthermore, direction suggested by the angle θ_2^{1P} is close to perpendicular to the direction given by the system of conjugated double bonds for all studied FPs fluorophores. All the reasons listed suggest that out of two mathematically possible TDM orientations only one of them, θ_1^{1P}, has a physical meaning.

Analysis of the z-stack measurement of mTurquoise FP crystal shown at the Figure 3.5 supports this conclusion. Here we define a half-penetration depth $d_{1/2}$ – an acquisition depth d within a FP crystal at which excitation light (and hence detected fluorescence) intensity I is half of the incident light (fluorescence at the very bottom layer of the crystal) intensity I_0:

$$d_{1/2} : \frac{I}{I_0} = \frac{1}{2}. \tag{3.14}$$

From the Equation 3.3 we then get dependence of half-penetration depth $d_{1/2}$ on the orientation of linear polarization of excitation light (given by angle α) and the possible TDM orientation (given by angle θ^{1P}):

$$d_{1/2}(\alpha, \theta^{1P}) = \frac{\log_{10}(2)}{C\varepsilon_{\text{cryst}}(\alpha, \theta^{1P})}. \tag{3.15}$$

From the z-stack measurement of mTurquoise FP crystal with incident light polarized parallelly to the long axis of the crystal ($\alpha = 90°$) we get that experimentally observed half-penetration depth in mTurquoise FP crystals is around 4 µm (see Figure 3.11).

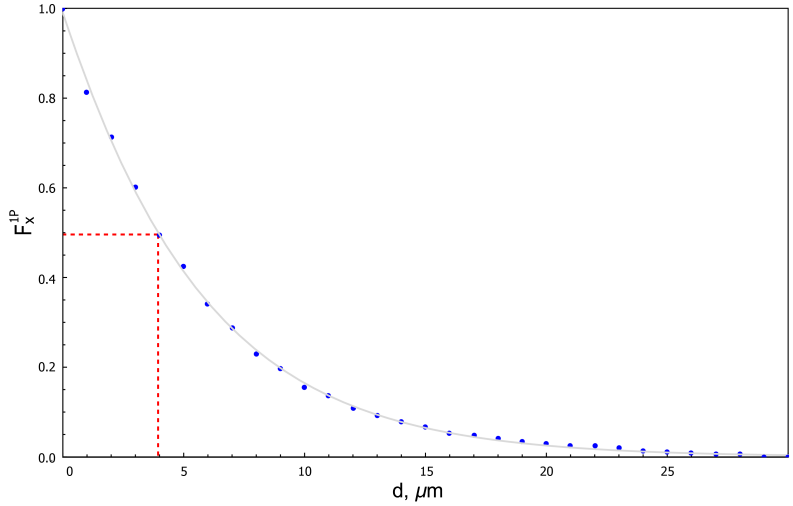

Figure 3.11: Experimental values F_x^{1P} of fluorescence intensity for the 1P excitation light polarized parallelly to the long axis of the crystal in the mTurquoise FP crystal shown at the Figure 3.5 acquired at different depths d within the crystal (deep blue dots). Experimental data is fitted with an exponential function (solid grey line). From the obtained fitting curve we get the value of half-penetration depth (defined in the Equation 3.14) in mTurquoise FP crystals: $d_{1/2} = 3.9\,\mu\text{m}$.

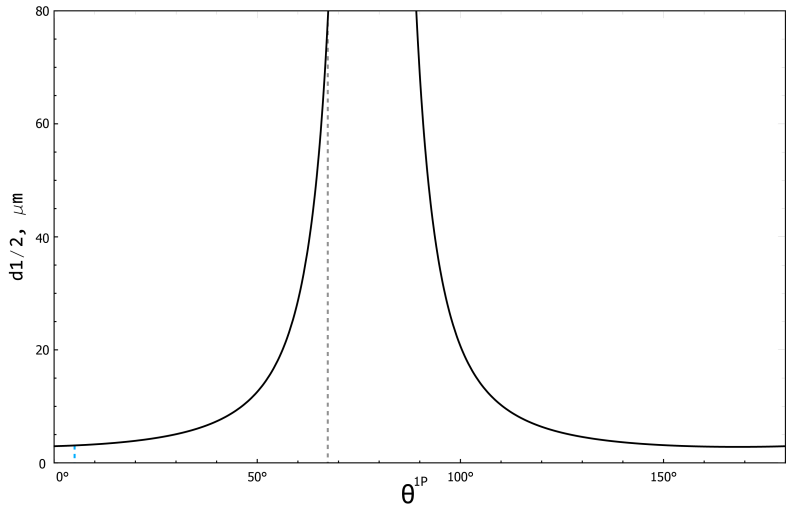

Figure 3.12: Figure shows dependence of half-penetration depth $d_{1/2}$ on the possible TDM orientation in mTurquoise FP crystals (solid black line). It was calculated for the polarization of 1P excitation light oriented parallelly to the long axis of the crystal using Equation 3.15. By comparing this dependence with two possible TDM orientations obtained from 1P polarization measurements (see Table 3.5), $\theta_1^{1P} = 5.0°$ (dashed blue line) and $\theta_2^{1P} = 67.4°$ (dashed grey line), we conclude that only one of them, θ_1^{1P}, corresponds to the half-penetration depth we observe in reality (c. 4 µm; see Figure 3.11).

If we then compare this experimental estimate with calculated dependence of half-penetration depth $d_{1/2}$ on the possible TDM orientation for vector $\vec{e} = \vec{e_x}$, i.e. $d_{1/2}(90°, \theta^{1P})$, using Equation 3.15, we see that only one out of two mathematically possible TDM orientations, namely θ_1^{1P}, corresponds to a half-penetration depth observed in actual polarization microscopy experiments. Therefore, analysis of our polarization microscopy imaging data in terms of half-penetration depth allows us to discard one of the two possible TDM orientations and hence unambiguously determination TDM orientations in studied FPs.

3.4 Vector-like behaviour of 2P absorption in studied FPs

Based on the comparison of our 1P and 2P polarization microscopy measurements, we hypothesized that 2P absorptivity tensors of studied FPs exhibit vector-like behaviour. In order to test this hypothesis, we have calculated 2PATs of studied FPs for their optimized fluorophores structures in vacuum using methods of molecular dynamics and QM calculations. Obtained 2PATs for the excitation from the ground electronic state to the first excited state have been diagonalized. Their eigenvalues are listed in the Table 3.6.

From Equation 1.6 it follows that the rate of absorption along an eigenvector depends on the square of the corresponding eigenvalue. Therefore, by comparing the calculated eigenvalues we get that the rate of absorption in directions perpendicular to the MARV (the eigenvector corresponding to the maximum eigenvalue of 2PAT) contributes less than 0.25%, 0.87% and 5.14% of the rate of absorption in the MARV direction in mTurquoise, eGFP and mCherry FPs respectively. From that we conclude that the influence of absorption cross sections on the rate of 2P absorption in directions perpendicular to the MARV can be safely neglected, and that anisotropy of 2P absorption in studied FPs does exhibit a vector-like behaviour.

Table 3.6: Results of QM calculations. Eigenvalues $\{S_i\}_{i=1}^{3}$ of calculated 2PATs for the $S_0 - S_1$ transition in mTurquoise, eGFP and mCherry FPs. The rate of absorption along an eigenvector depends on the square of the corresponding eigenvalue.

	mTurquoise	**eGFP**	**mCherry**
S_1	64.1	28.5	133.6
S_2	−3.2	−2.7	−30.3
S_3	0.3	0.6	0.2

3.5 Analysis of experimental data in terms of MARV orientations

Now that we have confirmed our assumption of vector-like behaviour of anisotropy of 2P absorption in the three studied FPs, we can implement it in our 2P polarization microscopy data analysis.

Similar approach has been used to obtain possible MARV orientations in the studied studied FPs. Theoretical dependencies of the ratio r^{2P} on the possible orientation of MARV ($\vec{\mu}^{2P}$) within the approximating plane of a fluorophore (defined by angle θ^{2P}) in studied FPs were calculated by rotating vector $\vec{\mu}^{2P}$ around the plane's normal $\vec{n_3}$ by angle θ^{2P} from the centreline $\vec{n_1}$ (see Figure 2.7) using Equation 2.7. Obtained theoretical curves $r^{2P}(\theta^{2P})$ are given in the Figure 3.13 for the three studied FPs.

Comparison of these theoretical dependencies $r^{2P}(\theta^{2P})$ with experimentally determined $\overline{r_{exp}^{2P}}$ values (see Table 3.4) gives us two possible MARV orientations, θ_1^{2P} and θ_2^{2P}, for each FP (see Figure 3.13). These orientations are listed in the Table 3.7 for the three studied FPs.

Table 3.7: Possible MARV orientations in studied FPs. For mTurquoise and eGFP FPs, possible MARV orientations, θ_1^{2P} and θ_2^{2P}, are given for $\overline{r_{exp}^{2P}}$, $\overline{r_{exp}^{2P}} \pm \sigma$ (68% confidence interval) and $\overline{r_{exp}^{2P}} \pm 2\sigma$ (95% confidence interval) values. For the FP of mCherry, θ_1^{2P} and θ_2^{2P} are given for the r_{exp}^{2P} value, since there was only one crystal measured.

FP	$\boldsymbol{r_{exp}^{2P}}$	$\boldsymbol{\theta_1^{2P}}$, °	$\boldsymbol{\theta_2^{2P}}$, °
mTurquoise	21.75	178.6	67.6
	21.75 + 5.74	6.4	67.2
	21.75 – 5.74	167.1	67.5
	21.75 + 2·5.74	12.0	67.1
	21.75 – 2·5.74	149.3	68.5
eGFP	16.51	5.5	76.7
	16.51 + 9.03	17.6	76.0
	16.51 – 9.03	159.5	77.9
	16.51 + 2·9.03	24.5	75.6
	16.51 – 2·9.03	–	–
mCherry	1.76	149.5	93.8

3.5.1 Multiple solutions

Mathematical analysis of our 2P polarization microscopy data gives two possible MARV orientations, θ_1^{2P} and θ_2^{2P}, for each FP (see Figure 3.13). Similarly to the possible TDM orientations, while both MARV orientations correspond the same value of r^{2P}, their calculated fluorescence intensity profiles significantly differ in magnitude (see Figure 3.14). Also, similar reasoning to the one given for distinguishing possible TDM orientations can be applied here, except for the half-penetration depth analysis due to the deeper penetration of 2P excitation light

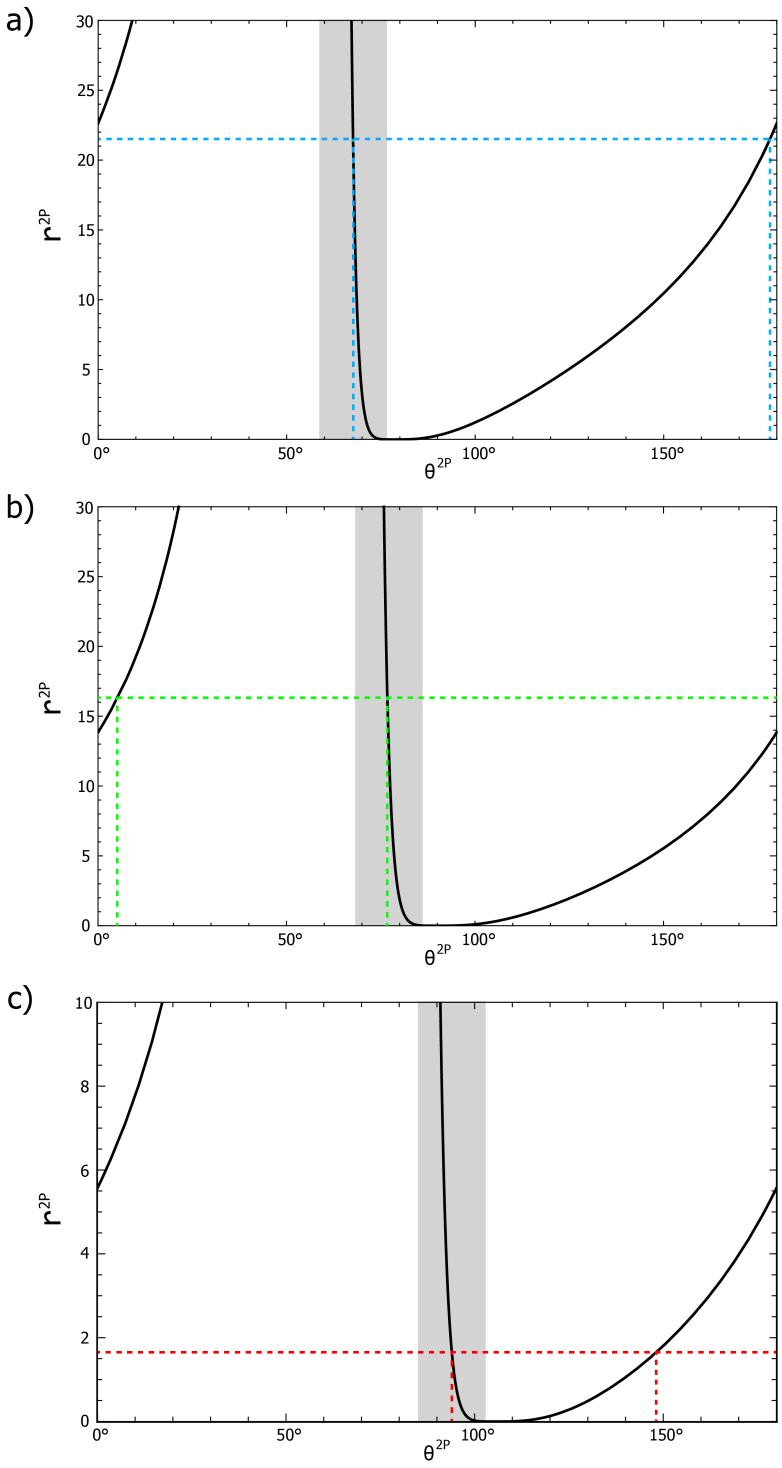

Figure 3.13: Possible MARV orientations in studied FPs. a), b), c) Calculated theoretical $r^{2P}(\theta^{2P})$ curves for mTurquoise, eGFP and mCherry FPs crystals respectively (solid black lines). An intercept of a theoretical curve with a horizontal line corresponding to the experimentally determined $\overline{r^{2P}_{exp}}$ value (coloured dashed lines) gives two possible MARV orientations, θ^{2P}_1 and θ^{2P}_2, for each FP. Grey shaded areas highlight regions of rapid change of r^{2P} ratio. MARV orientations obtained in these regions are labelled θ^{2P}_2 in the Table 3.7.

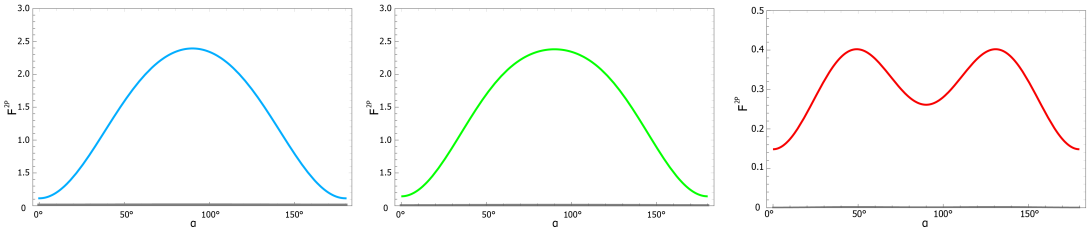

Figure 3.14: Calculated dependencies of fluoresce intensities for 2P excitation F^{2P} (see Equation 2.3) on the orientation of polarization of excitation light (given by angle α) in mTurquoise (left), eGFP (centre) and mCherry (right) FPs for two possible MARV orientations, θ_1^{2P} (coloured lines) and θ_2^{2P} (grey lines).

into the sample. Therefore, even though we cannot implement half-penetration depth analysis in order to unambiguously experimentally distinguish in between two possible MARV orientations, θ_1^{2P} and θ_2^{2P}, due to the similarity of the problem with the 1P case, we conclude that only one MARV orientation, θ_1^{2P}, corresponds to the physical process of absorption in the studied FPs.

3.6 Final results

As a result of our polarization microscopy measurements and mathematical analysis we have unambiguously determined TDM and MARV orientations in the three studied FPs (see Figure 3.15). Obtained values of angles θ^{1P} and θ^{2P} are listed in the Table 3.8. Consistence of our TDM orientations with QM predictions given in Ansbacher et al. [2012] gives us certainty in the results obtained.

Table 3.8: Obtained TDM and MARV orientations in studied FPs. For each FP, selected TDM (θ^{1P}) and MARV (θ^{2P}) orientations are listed. In the third column QM predictions for TDM orientations described in Ansbacher et al. [2012] are given.

FP	$\boldsymbol{\theta^{1P}}$**, °**	**QM, °**	$\boldsymbol{\theta^{2P}}$**, °**
mTurquoise	5.0	176.8	178.6
eGFP	179.5	10.8	5.5
mCherry	152.8	159.8	149.5

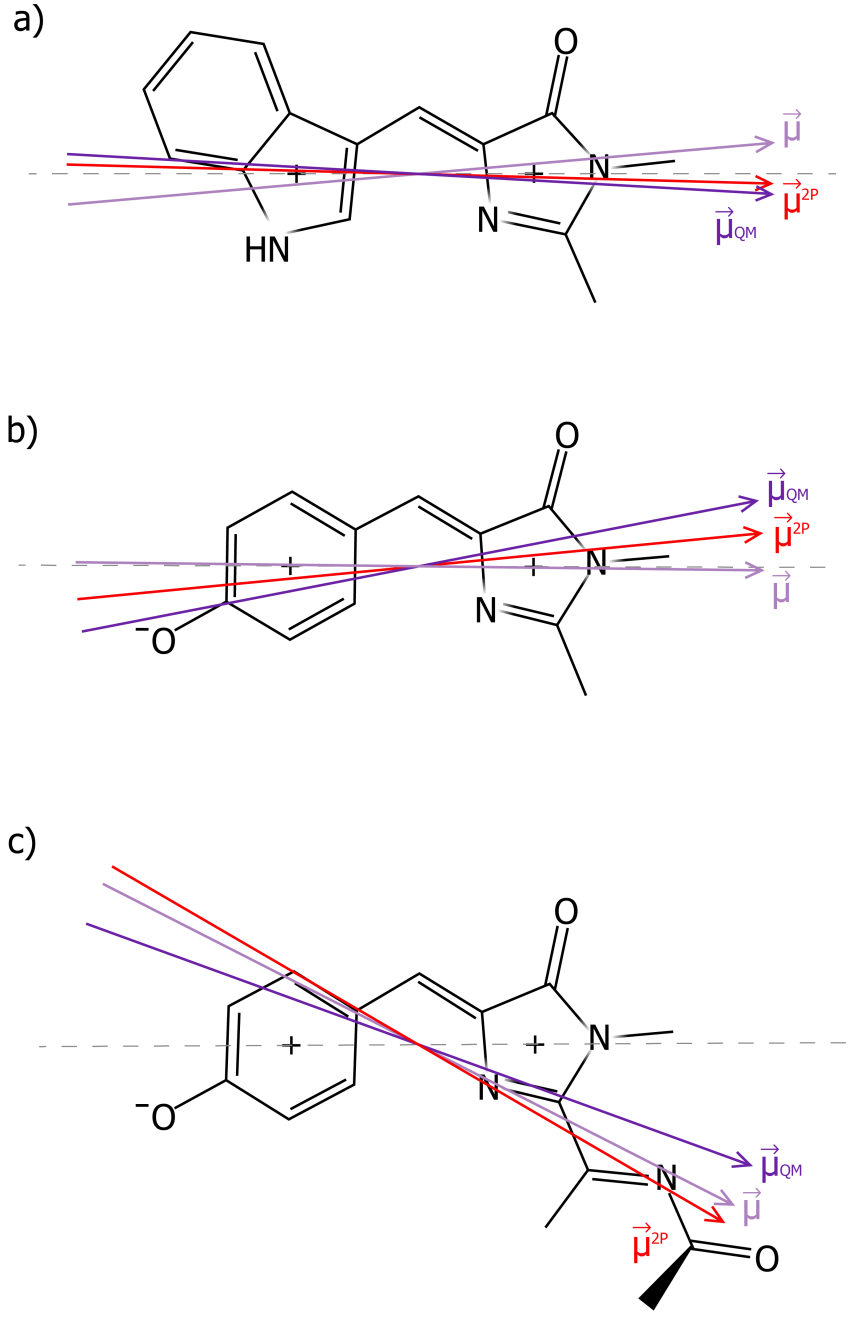

Figure 3.15: a), b), c) Graphical representation of obtained TDM ($\vec{\mu}$, in light violet) and MARV ($\vec{\mu}^{2P}$, in red) orientations within the approximating plane of a fluorophore for mTurquoise, eGFP and mCherry FPs respectively. QM predictions of TDM orientations given at Ansbacher et al. [2012], $\vec{\mu}_{QM}$, are shown in deep violet. Dashed grey lines represent centrelines of fluorophores, i.e. lines connecting centres of two aromatic rings.

4. Discussion

Our results show that it is in principle possible to determine TDM orientations in FPs by combining X-ray crystallography and optical microscopy measurements. From mathematical analysis of our polarization microscopy measurements we obtain two possible TDM orientations. By performing additional optical measurements of light penetration depth within FPs crystals, we are able to distinguishing between the two possibilities and unambiguously determine TDM orientations in studied FPs.

For accurate TDM orientation determinations, using measurements of fluorescence intensity is complicated by high molar attenuation coefficient of FPs crystals, which causes the intensity of the illuminating light to change during passing through the crystal differently for different polarizations. That is why we made *mixed* crystals of fluorescent and mutated, non-fluorescent proteins that allowed us to obtain more consistent results. Such crystals promise to yield accurate information on TDM orientation. Despite difficulties with the high light absorption by FP crystals, we were able to determine TDM orientations in three widely used FPs: mTurquoise, eGFP and mCherry.Consistence with QM predictions given in Ansbacher et al. [2012] gives us certainty in the obtained results.

While QM calculations have yielded complete information on absorptivity tensors, the accuracy of in silico QM results and the extent of their agreement with experimental data is somewhat uncertain. Also, further testing of performed QM calculations against more expensive high-accuracy methods is needed. In contrast, 2P polarization microscopy measurements provided information on in vitro behaviour of real FP molecules. However, this information was interpreted using a vector-like approximation of the 2PAT. Also, the half-penetration depth analysis used for distinguishing in between two possible TDM orientations cannot be applied in case of 2P absorption, in principle leaving us with two possible MARV orientations.

It is important to notice several assumptions that have been made during the course of this work. First, that TDMs/MARVs of studied FPs are lying within the approximating plane of a fluorophore. Second, that fluorescent protein crystals are lying exactly flat within the plane of the slide during polarization microscopy measurements (however, our calculations – not shown here – prove that rotations within 10° around the long axis of the crystal do not have a sufficient effect on TDM/MARV orientation determinations in the three FPs crystals of given crystallographic space groups. More significant rotations would be visible during polarization microscopy measurements and would be corrected for). Finally, the most crucial part of the performed mathematical analysis is the accurate knowledge of the crystallographic axes orientations with respect to the macroscopic environment. In this thesis, for the orientation of crystallographic axes within mTurquoise and eGFP crystals we have used the assumption made in Rosell and Boxer [2003]. However, our recent, more accurate X-ray diffraction measurements (see *Additional X-ray diffraction measurements*) let us assume that this might not be exactly correct. Nevertheless, our new X-diffraction measurements haven't been performed on the crystals used in this thesis, and therefore this new information hasn't been included into the mathematical analysis in this thesis.

5. Conclusion

In this thesis, we have performed a combination of experiments involving methods of molecular biology, biochemistry, advanced microscopy, image analysis and mathematical modelling. This allowed us to characterize the TDMs and 2PATs of three studied FPs. Several goals have been achieved:

1. We have purified and crystallized FPs of interest.
2. Employing X-ray crystallography, we have established crystallographic space groups of studied FP crystals. For mCherry FP crystals, we have as well determined FP orientations within the crystal.
3. We have performed extensive 1P polarization microscopy measurements on FP crystals. During these experiments, we have faced and managed to overcome difficulties caused by a high molar attenuation coefficient of FP crystals by co-crystallizing mTurquoise FP with its non-fluorescent mutant mTurquoiseW67A and proving that physically diluting fluorophore concentration in FP crystal is equivalent to performing measurements at the edge of the excitation spectrum of corresponding FP.
4. We have performed equivalent optical experiments using 2P excitation.
5. By the means of QM calculations we have proved our hypothesis that anisotropy of 2P absorption of studied FPs can be described by a vector (MARV) rather than a tensor (2PAT).
6. Based on this assumption and by virtue of knowing structures and orientations of the studied FP molecules, we were able to interpret results of our polarization microscopy measurements in terms of TDM and MARV orientations.

The results of our work contribute to the knowledge of optical properties of three fluorescent proteins – mTurquoise, eGFP and mCherry.

Bibliography

Tamar Ansbacher, Hemant Kumar Srivastava, Tamar Stein, Roi Baer, Maarten Merkx, and Avital Shurki. Calculation of transition dipole moment in fluorescent proteins—towards efficient energy transfer. *Physical Chemistry Chemical Physics*, 14(12):4109–4117, February 2012. ISSN 1463-9084. doi: 10.1039/C2CP23351G. URL https://pubs.rsc.org/en/content/articlelanding/2012/cp/c2cp23351g.

Robert E. Campbell. Fluorescent proteins. *Scholarpedia*, 3(7):5410, July 2008. ISSN 1941-6016. doi: 10.4249/scholarpedia.5410. URL http://www.scholarpedia.org/article/Fluorescent_proteins.

Brendan P. Cormack, Raphael H. Valdivia, and Stanley Falkow. FACS-optimized mutants of the green fluorescent protein (GFP). *Gene*, 173(1):33–38, January 1996. ISSN 0378-1119. doi: 10.1016/0378-1119(95)00685-0. URL http://www.sciencedirect.com/science/article/pii/0378111995006850.

Mikhail Drobizhev, Nikolay S. Makarov, Shane E. Tillo, Thomas E. Hughes, and Aleksander Rebane. Two-photon absorption properties of fluorescent proteins. *Nature Methods*, 8(5):393–399, May 2011. ISSN 1548-7105. doi: 10.1038/nmeth.1596. URL https://www.nature.com/articles/nmeth.1596.

Chong Fang, Renee R. Frontiera, Rosalie Tran, and Richard A. Mathies. Mapping GFP structure evolution during proton transfer with femtosecond Raman spectroscopy. *Nature*, 462(7270):200–204, November 2009. ISSN 1476-4687. doi: 10.1038/nature08527. URL https://www.nature.com/articles/nature08527/.

Arno Germond, Hideaki Fujita, Taro Ichimura, and Tomonobu M. Watanabe. Design and development of genetically encoded fluorescent sensors to monitor intracellular chemical and physical parameters. *Biophysical Reviews*, 8(2):121–138, June 2016. ISSN 1867-2469. doi: 10.1007/s12551-016-0195-9. URL https://doi.org/10.1007/s12551-016-0195-9.

Joachim Goedhart, Laura van Weeren, Mark A. Hink, Norbert O. E. Vischer, Kees Jalink, and Theodorus W. J. Gadella. Bright cyan fluorescent protein variants identified by fluorescence lifetime screening. *Nature Methods*, 7(2):137–139, February 2010. ISSN 1548-7105. doi: 10.1038/nmeth.1415. URL https://www.nature.com/articles/nmeth.1415.

Maria Khrenova, Igor Topol, Jack Collins, and Alexander Nemukhin. Estimating Orientation Factors in the FRET Theory of Fluorescent Proteins: The TagRFP-KFP Pair and Beyond. *Biophysical Journal*, 108(1):126–132, January 2015. ISSN 0006-3495. doi: 10.1016/j.bpj.2014.11.1859. URL http://www.sciencedirect.com/science/article/pii/S0006349514030719.

Joseph R. Lakowicz. *Topics in Fluorescence Spectroscopy: Nonlinear and Two-Photon-Induced Fluorescence*. Springer Science & Business Media, 1991. ISBN 9780306455537. Google-Books-ID: QxzscM0htSAC.

Joseph R. Lakowicz. *Principles of Fluorescence Spectroscopy*. Springer US, 3 edition, 2006. ISBN 9780387312781. doi: 10.1007/978-0-387-46312-4. URL https://www.springer.com/gp/book/9780387312781.

Josef Lazar, Alexey Bondar, Stepan Timr, and Stuart J. Firestein. Two-photon polarization microscopy reveals protein structure and function. *Nature Methods*, 8(8):684–690, August 2011. ISSN 1548-7105. doi: 10.1038/nmeth.1643. URL https://www.nature.com/articles/nmeth.1643.

T. A. Masters, R. J. Marsh, T. S. Blacker, D. A. Armoogum, B. Larijani, and A. J. Bain. Polarized two-photon photoselection in egfp: Theory and experiment. *The Journal of Chemical Physics*, 148(13):134311, 2018. doi: 10.1063/1.5011642. URL https://doi.org/10.1063/1.5011642.

David W. Piston and Gert-Jan Kremers. Fluorescent protein FRET: the good, the bad and the ugly. *Trends in Biochemical Sciences*, 32(9):407–414, September 2007. ISSN 0968-0004. doi: 10.1016/j.tibs.2007.08.003. URL http://www.sciencedirect.com/science/article/pii/S0968000407001910.

Douglas C. Prasher, Virginia K. Eckenrode, William W. Ward, Frank G. Prendergast, and Milton J. Cormier. Primary structure of the Aequorea victoria green-fluorescent protein. *Gene*, 111(2):229–233, February 1992. ISSN 0378-1119. doi: 10.1016/0378-1119(92)90691-H. URL http://www.sciencedirect.com/science/article/pii/037811199290691H.

Erik A. Rodriguez, Robert E. Campbell, John Y. Lin, Michael Z. Lin, Atsushi Miyawaki, Amy E. Palmer, Xiaokun Shu, Jin Zhang, and Roger Y. Tsien. The Growing and Glowing Toolbox of Fluorescent and Photoactive Proteins. *Trends in Biochemical Sciences*, 42(2):111–129, February 2017. ISSN 0968-0004. doi: 10.1016/j.tibs.2016.09.010. URL http://www.sciencedirect.com/science/article/pii/S0968000416301736.

Federico I. Rosell and Steven G. Boxer. Polarized Absorption Spectra of Green Fluorescent Protein Single Crystals: Transition Dipole Moment Directions. *Biochemistry*, 42(1):177–183, January 2003. ISSN 0006-2960. doi: 10.1021/bi0266535. URL https://doi.org/10.1021/bi0266535.

Nathan C. Shaner, Robert E. Campbell, Paul A. Steinbach, Ben N. G. Giepmans, Amy E. Palmer, and Roger Y. Tsien. Improved monomeric red, orange and yellow fluorescent proteins derived from Discosoma sp. red fluorescent protein. *Nature Biotechnology*, 22(12):1567–1572, December 2004. ISSN 1546-1696. doi: 10.1038/nbt1037. URL https://www.nature.com/articles/nbt1037.

Xiaokun Shu, Nathan C. Shaner, Corinne A. Yarbrough, Roger Y. Tsien, and S. James Remington. Novel Chromophores and Buried Charges Control Color in mFruits,. *Biochemistry*, 45(32):9639–9647, August 2006. ISSN 0006-2960. doi: 10.1021/bi060773l. URL https://doi.org/10.1021/bi060773l.

Chen Sy and Van Der Meer Bw. Theory of two-photon induced fluorescence anisotropy decay in membranes. *Biophysical Journal*, 64(5):1567–1575, May 1993. ISSN 0006-3495, 1542-0086. doi: 10.1016/s0006-3495(93)81526-1. URL https://europepmc.org/article/med/19431897.

Štepán Timr, Jirí Brabec, Alexey Bondar, Tomáš Ryba, Miloš Železný, Josef Lazar, and Pavel Jungwirth. Nonlinear Optical Properties of Fluorescent Dyes Allow for Accurate Determination of Their Molecular Orientations in Phospholipid Membranes. *The Journal of Physical Chemistry B*, 119(30):9706–9716, July 2015. ISSN 1520-6106. doi: 10.1021/acs.jpcb.5b05123. URL https://doi.org/10.1021/acs.jpcb.5b05123.

A. Ustione and D. W. Piston. A simple introduction to multiphoton microscopy. *Journal of Microscopy*, 243(3):221–226, 2011. ISSN 1365-2818. doi: 10.1111/j.1365-2818.2011.03532.x. URL https://onlinelibrary.wiley.com/doi/abs/10.1111/j.1365-2818.2011.03532.x.

List of Abbreviations

FP	fluorescent protein
PDB	protein data bank
GFP	green fluorescent protein
wtGFP	wild-type green fluorescent protein
eGFP	enhanced green fluorescent protein
YFP	yellow fluorescent protein
CFP	cyan fluorescent protein
FRET	Förster resonance energy transfer
1P	one-photon
TDM	transition dipole moment
2P	two-photon
2PAT	two-photon absorptivity tensor
MARV	maximum absorption rate vector
IPTG	isopropyl β-d-1-thiogalactopyranoside
PEG	polyethylene glycol
HEPES	4-(2-hydroxyethyl)-1-piperazineethanesulfonic acid
FPLC	fast protein liquid chromatography
SDS-PAGE	sodium dodecyl sulfate–polyacrylamide gel electrophoresis
ML	mother liquor
NMWL	nominal molecular weight limit
QM	quantum mechanical
PMT	photomultiplier tubes
PCR	polymerase chain reaction

List of Figures

1.1 Jablonski diagram . . . 3
1.2 Spectral variants of FPs . . . 4
1.3 Information on wtGFP (PDB: 1EMB) . . . 5
1.4 Spectral information on the studied FPs . . . 6
1.5 Structural information on the fluorophores of studied FPs . . . 7
1.6 Anisotropy of light absorption by FPs . . . 9
1.7 FP crystals allow for structural and orientational analysis . . . 9
1.8 Jablonski diagram for 1P and 2P absorption . . . 10
1.9 Orientational dependence of 1P absorption rate . . . 11
1.10 Possible shapes of 2P absorption cross section . . . 12
1.11 Orientational dependence of 2P absorption rate (MARV approximation) . . . 13

2.1 ÄKTA FPLC protein purification setup . . . 15
2.2 Example of a protein purification run . . . 16
2.3 Hanging drop vapour diffusion crystallization method . . . 17
2.4 1P polarization microscopy setup . . . 19
2.5 2P polarization microscopy setup . . . 19
2.6 Illustration of 1P polarization microscopy measurement . . . 20
2.7 Multiple coordinate systems . . . 21

3.1 Structural information on obtained FPs crystals . . . 25
3.2 Experimental curves of 1P polarization microscopy measurements 27
3.3 Experimental curves of 2P polarization microscopy measurements 29
3.4 Possible TDM orientations in studied FPs . . . 31
3.5 z-stack measurement of mTurquoise FP crystal . . . 32
3.6 Uneven light penetration within the depth of FP crystal . . . 33
3.7 Light penetration and FP fluorophore concentration . . . 34
3.8 Non-fluorescent mutant of mTurquoise FP . . . 35
3.9 Comparison of r_{exp}^{1P} values for normal and *mixed* FP crystals . . . 36
3.10 Comparison of two possible TDM orientations . . . 37
3.11 Experimental determination of $d_{1/2}$ . . . 38
3.12 Analysis of $d_{1/2}$ in terms of TDM orientations . . . 38
3.13 Possible MARV orientations in studied FPs . . . 41
3.14 Comparison of two possible MARV orientations . . . 42
3.15 Obtained TDM and MARV orientations in studied FPs . . . 43

A.1 Mutant mTurquoiseW67A plasmid map . . . 62
A.2 SDS-page gel image . . . 62
A.3 Crystallization drop images . . . 63
A.4 Negative control of mTurquoiseW67A protein fluorescence . . . 63
A.5 X-ray diffractometry setup . . . 64

List of Tables

2.1 Crystallization conditions 17
2.2 Parameters of FPs approximating fluorophore planes 22

3.1 Quantitative information on crystallographic space groups 24
3.2 List of space group symmetry operations 25
3.3 Values of $\overline{r_{exp}^{1P}}$ for studied FPs 26
3.4 Values of $\overline{r_{exp}^{2P}}$ for studied FPs 28
3.5 Possible TDM orientations in studied FPs 30
3.6 Results of QM calculations 39
3.7 Possible MARV orientations in studied FPs 40
3.8 Final results 42

A.1 Values of r_{exp}^{1P} obtained for *mixed* mTurquoise FP crystals 52
A.2 Values of r_{exp}^{1P} obtained for mTurquoise FP crystals 53
A.3 Values of r_{exp}^{1P} obtained for eGFP crystals 54
A.4 Values of r_{exp}^{1P} obtained for mCherry FP crystals 55
A.5 Values of r_{exp}^{2P} obtained for studied FPs crystals 56
A.6 Optimized fluorophore coordinates of mTurquoise FP 57
A.7 Optimized fluorophore coordinates of eGFP 58
A.8 Optimized fluorophore coordinates of mCherry FP 59

A. Attachments

A.1 Values of r_{exp}^{1P} obtained for individual crystals

A.1.1 mTurquoise FP

Table A.1: *Mixed* mTurquoise FP crystals have been measured at two excitation wavelengths, 405 nm and 488 nm. For each crystal measurement, a r_{exp}^{1P} value and a corresponding adjusted R^2 value describing the goodness of the fit are listed.

405 nm		488 nm	
r_{exp}^{1P}	R^2	r_{exp}^{1P}	R^2
5.40	0.9977	5.32	0.9950
5.24	0.9988	5.03	0.9985
5.30	0.9979	5.16	0.9981
5.24	0.9982	5.26	0.9944
4.92	0.9989	4.95	0.9995
5.13	0.9983	5.20	0.9994
5.11	0.9975	5.04	0.9982
5.20	0.9985	5.16	0.9994
5.13	0.9974	5.06	0.9982
4.91	0.9991	5.08	0.9987
4.89	0.9987	5.12	0.9993
4.93	0.9991	5.04	0.9994
5.02	0.9984	5.04	0.9987
5.79	0.9987	5.46	0.9991
4.98	0.9975	5.04	0.9993
5.12	0.9979	5.09	0.9986
5.25	0.9984	5.30	0.9975
4.83	0.9974	4.79	0.9976
5.58	0.9962	5.27	0.9970
5.95	0.9984	5.61	0.9981
5.12	0.9990	5.03	0.9980
5.46	0.9970	5.38	0.9970
5.46	0.9985	4.94	0.9994
5.23	0.9987	4.92	0.9990

Table A.2: mTurquoise FP crystals have been measured at two excitation wavelengths, 405 nm and 488 nm. For each crystal measurement, a r_{exp}^{1P} value and a corresponding adjusted R^2 value describing the goodness of the fit are listed.

405 nm		488 *nm*	
$\boldsymbol{r_{exp}^{1P}}$	$\boldsymbol{R^2}$	$\boldsymbol{r_{exp}^{1P}}$	$\boldsymbol{R^2}$
2.56	0.9991	4.58	0.9933
2.71	0.9996	5.45	0.9957
2.30	0.9965	5.29	0.9970
2.59	0.9992	4.80	0.9981
2.73	0.9991	5.14	0.9973
2.73	0.9997	5.50	0.9996
2.45	0.9997	5.70	0.9987
2.43	0.9994	5.60	0.9981
1.55	0.9978	5.71	0.9976
2.12	0.9975	6.64	0.9963
1.67	0.9926	6.76	0.9983
2.73	0.9958	5.59	0.9986
1.82	0.9926	5.81	0.9993
2.92	0.9927	5.09	0.9961
2.52	0.9945	5.90	0.9923
2.43	0.9973	5.06	0.9944
3.76	0.9947	5.74	0.9928
2.63	0.9953	5.31	0.9999
2.16	0.9969	4.96	0.9958
2.67	0.9990	4.96	0.9949
3.65	0.9979	5.24	0.9994
2.60	0.9978	5.30	0.9951
1.90	0.9982	4.88	0.9984
3.53	0.9976	6.03	0.9957
2.77	0.9987	5.95	0.9961
2.63	0.9990	6.15	0.9974
4.22	0.9910	5.30	0.9938
3.26	0.9980	5.78	0.9992
3.20	0.9959	6.51	0.9991
2.27	0.9831	5.69	0.9948
3.43	0.9831	5.60	0.9968
2.49	0.9983	5.90	0.9963
3.66	0.9989	5.89	0.9976
3.51	0.9994	6.21	0.9904
3.03	0.9957	6.44	0.9993
2.94	0.9902	5.90	0.9991
4.35	0.9871	6.89	0.9981
2.21	0.9980	5.25	0.9989

A.1.2 eGFP

Table A.3: eGFP crystals have been measured at two excitation wavelengths, 405 nm and 488 nm. For each crystal measurement, a r_{exp}^{1P} value and a corresponding adjusted R^2 value describing the goodness of the fit are listed.

405 nm		488 nm	
$\boldsymbol{r_{exp}^{1P}}$	$\boldsymbol{R^2}$	$\boldsymbol{r_{exp}^{1P}}$	$\boldsymbol{R^2}$
4.96	0.9987	1.76	0.9917
4.57	0.9987	2.46	0.9995
4.37	0.9982	2.35	0.9995
4.52	0.9997	2.62	0.9973
4.00	0.9990	2.30	0.9980
3.04	0.9998	2.15	0.9990
3.08	0.9997	2.02	0.9999
3.72	0.9993	2.21	0.9996
3.90	0.9990	2.38	0.9997
3.23	0.9994	1.99	0.9998
3.97	0.9994	2.32	0.9995
3.65	0.9887	2.06	0.9988
3.49	0.9926	2.09	0.9988
3.30	0.9992	1.98	0.9987
4.66	0.9990	2.44	0.9991
2.86	0.9996	1.03	0.9996
3.47	0.9992	1.57	0.9993
3.24	0.9991	1.37	0.9994
4.22	0.9990	1.98	0.9973
3.67	0.9989	1.56	0.9984
3.08	0.9995	1.29	0.9996
2.94	0.9996	1.24	0.9999
4.45	0.9993	1.73	0.9999
5.25	0.9986	2.12	0.9990
5.23	0.9977	2.36	0.9994
3.41	0.9965	1.73	0.9988
4.06	0.9997	1.42	0.9998
2.44	0.9998	1.59	0.9994
2.75	0.9998	1.45	0.9991
3.18	0.9967	1.12	0.9996
3.75	0.9993	1.16	0.9995
2.90	0.9997	2.25	0.9999
4.15	0.9998	1.12	0.9995
2.89	0.9998	1.18	0.9997
3.72	0.9996	1.96	0.9989
3.62	0.9989	2.10	0.9971
2.73	0.9999	1.61	0.9992
2.74	0.9987	2.83	0.9968

4.61	0.9979	2.54	0.9976
3.06	0.9983	2.84	0.9984
6.18	0.9972	1.64	0.9974
5.91	0.9964		

A.1.3 mCherry FP

Table A.4: mCherry FP crystals have been measured at 515 nm excitation wavelength. For each crystal measurement, a r_{exp}^{1P} value and a corresponding adjusted R^2 value describing the goodness of the fit are listed.

515 nm	
$\boldsymbol{r_{exp}^{1P}}$	$\boldsymbol{R^2}$
1.37	0.9995
1.23	0.9998
1.03	0.9997
1.37	0.9999
1.37	0.9998
1.37	0.9998
2.02	0.9998
1.94	0.9998

A.2 Values of r_{exp}^{2P} obtained for individual crystals

Table A.5: Values of r_{exp}^{2P} obtained for studied FPs crystals. mTurquoise and eGFP crystals have been measured at 810 nm excitation wavelength. mCherry FP crystals have been measured at 960 nm excitation wavelength. For each crystal measurement, a r_{exp}^{2P} value and a corresponding adjusted R^2 value describing the goodness of the fit are listed.

mTurquoise		**eGFP**		**mCherry**	
810 nm		810 nm		960 nm	
r_{exp}^{2P}	R^2	r_{exp}^{2P}	R^2	r_{exp}^{2P}	R^2
20.05	0.8905	10.47	0.9061	1.76	0.9963
17.47	0.9656	23.04	0.8570		
20.57	0.9711	6.68	0.9921		
18.28	0.9736	18.08	0.8760		
20.39	0.9886	20.02	0.9620		
32.88	0.9989	34.69	0.9520		
21.18	0.9860				
15.98	0.9970				
26.81	0.9730				
20.82	0.9247				
25.10	0.9433				
35.07	0.9969				
16.74	0.9972				

A.3 Optimized fluorophores coordinates of studied FPs

A.3.1 mTurquoise FP

Table A.6: Results of geometry optimization of mTurquoise FP fluorophore molecule in vacuum performed in Gaussian16 software package using Hartree-Fock functional and 6-31G basis set. Coordinates are given in atomic units. These coordinates were then used for QM calculations of 2PAT for the $S_0 - S_1$ transition in DALTON software package.

N	–0.077	0.000	–0.042
C	0.234	0.000	1.340
C	1.127	0.000	–0.761
C	1.708	0.000	1.356
N	2.188	0.000	0.019
C	1.177	0.000	–2.254
C	–1.443	0.000	–0.541
O	–0.607	0.000	2.264
C	2.468	0.000	2.487
C	3.895	0.000	2.574
H	0.181	0.000	–2.700
H	1.718	0.882	–2.614
H	1.718	–0.882	–2.614
H	–2.096	0.000	0.335
H	–1.653	0.893	–1.140
H	–1.653	–0.893	–1.140
C	4.686	0.000	3.800
C	6.056	0.000	3.416
N	6.088	0.000	2.019
C	4.805	0.000	1.518
C	7.099	0.000	4.347
C	6.752	0.000	5.699
C	5.400	0.000	6.104
C	4.366	0.000	5.168
H	1.913	0.000	3.423
H	6.924	0.000	1.458
H	4.585	0.000	0.463
H	8.139	0.000	4.035
H	7.535	0.000	6.450

A.3.2 eGFP

Table A.7: Results of geometry optimization of eGFP fluorophore molecule in vacuum performed in Gaussian16 software package using Hartree-Fock and B3LYP functionals and 6-31G basis set. Coordinates are given in atomic units. These coordinates were then used for QM calculations of 2PAT for the $S_0 - S_1$ transition in DALTON software package.

O	–0.121	0.000	0.005
C	0.014	0.000	1.263
N	1.280	0.000	1.910
C	2.528	0.000	1.173
H	3.370	0.000	1.868
H	2.595	–0.884	0.527
H	2.595	0.884	0.527
C	1.065	0.000	3.296
C	2.169	0.000	4.299
H	1.719	0.000	5.294
H	2.815	–0.885	4.210
H	2.815	0.885	4.210
N	–0.218	0.000	3.595
C	–0.931	0.000	2.368
C	–2.311	0.000	2.200
H	–2.609	0.000	1.150
C	–3.368	0.000	3.132
C	–4.724	0.000	2.653
C	–5.803	0.000	3.499
C	–5.645	0.000	4.947
C	–4.265	0.000	5.415
C	–3.192	0.000	4.561
O	–6.644	0.000	5.748
H	–4.880	0.000	1.574
H	–6.820	0.000	3.118
H	–4.121	0.000	6.492
H	–2.174	0.000	4.938
H	5.164	0.000	7.163
H	3.331	0.000	5.496

A.3.3 mCherry FP

Table A.8: Results of geometry optimization of mCherry fluorophore molecule in vacuum performed in Gaussian16 software package using Hartree-Fock functional and 6-31G basis set. Coordinates are given in atomic units. These coordinates were then used for QM calculations of 2PAT for the $S_0 - S_1$ transition in DALTON software package.

N	0.004	–0.062	–0.484
C	–0.132	–0.106	0.881
C	1.173	–0.241	1.474
N	2.036	–0.270	0.393
C	1.272	–0.158	–0.773
C	–1.311	–0.042	1.628
C	–2.635	0.082	1.261
C	–3.105	0.184	–0.096
C	–4.416	0.300	–0.389
C	–5.441	0.330	0.642
C	–4.961	0.229	2.010
C	–3.646	0.113	2.286
O	–6.654	0.437	0.371
O	1.524	–0.317	2.669
C	3.470	–0.385	0.558
C	1.761	–0.143	–2.131
C	0.738	0.089	–3.215
N	3.019	–0.341	–2.340
C	3.657	–0.236	–3.562
O	3.342	0.538	–4.461
C	4.865	–1.121	–3.681
H	3.981	0.457	0.116
H	3.655	–0.409	1.620
H	3.845	–1.286	0.099
H	0.956	–0.514	–4.084
H	–0.250	–0.126	–2.848
H	0.780	1.123	–3.532
H	5.303	–1.022	–4.663
H	5.591	–0.845	–2.926
H	4.590	–2.153	–3.499
H	–1.121	–0.105	2.687
H	–2.374	0.166	–0.879
H	–4.757	0.377	–1.404
H	–5.700	0.251	2.787
H	–3.322	0.040	3.310

A.4 Examples of Wolfram Mathematica code

In[1]:=
```
(*find approximating plane of a fluorophore*)
ss[a_, b_, c_, d_] =
Block[{x = data[[All, 1]], y = data[[All, 2]],
z = data[[All, 3]], res}, res =
(a*x + b*y + c*z + d)/(a^2 + b^2 + c^2)^0.5; res.res];
Minimize[ss[a, b, c, d], {a, b, c, d}];
(*a,b,c,d - parameters of the plane*)
{a, b, c, d} = {a, b, c, d} /. Last[%];
(*n3 - normal to the plane*)
n3 = Normalize[{a, b, c}];
```

In[2]:=
```
(*project atoms coordinates onto the approximating plane
of a fluorophore: basically find points {x,y,z}
that belong both to the plane ax+by+cz+d=0 and to
the plane normal that goes through original point {X,Y,Z}
that we want to project: c(x-X)=a(z-Z),b(x-X)=a(y-Y)*)
planarcoordinates = Table[{0, 0, 0}, {i, 1, k}];
M = {{c, 0, -a}, {b, -a, 0}, {a, b, c}};
Do[V = {c*data[[i, 1]] - a*data[[i, 3]], b*data[[i, 1]]
- a*cd[[i, 2]], -d};
(*obtained planar coordinates*)
planarcoordinates[[i, ;;]] =
LinearSolve[M, V], {i, 1, k}];
```

In[3]:=
```
(*mTurquoise2 4AR7*)
n1 = {-0.8749375114079091`, -0.4010838949569906`,
0.27132279730510045`};
n3 = {-0.44907905988256613`, 0.8816802603960372`,
-0.14480302622171545`};
```

In[4]:=
```
(*eGFP (2Y0G)*)
n1= {-0.8830282613024489`, -0.4578152703120305`,
0.10327762589397815`};
n3= {-0.46927440432222867`, 0.8643602343689064`,
-0.18072885405973946`};
```

In[5]:=
```
(*mCherry (2H5Q)*)
n1 = {0.8307885314710669`, -0.5408453007785068`,
-0.13144115261954561`};
n3= {-0.5090372111593384`, -0.8338300484537061`,
0.21356162565127043`};
```

In[6]:=
```
(*e - electric field vector, at start parallel to y axis,
then rotated in the counter-clockwise direction by angle
alpha in xy plane around z axis*)
e[alpha_] =
RotationMatrix[alpha*Pi/180, {0, 0, 1}].{0, 1, 0};
```

In[7]:=
```
(*possible TDM/MARV orientation is given by angle theta;
at start TDM/MARV is parallel to the centreline n1,
then rotated in the counter-clockwise direction by angle
theta in the approximating fluorophore plane around
plane's normal n3*)
tdm[theta_] = RotationMatrix[theta*Pi/180, n3].n1;

(*there are several FP molecules in a unit cell*)
(*four unique orientations in P212121 space group*)
N = 4;
tdmspacegroup[theta_] = {tdm[theta], {-1, -1, 1}*tdm[theta],
{-1, 1, -1}*tdm[theta], {1, -1, -1}* tdm[theta]};
(*two unique orientations in P21 space group*)
N = 2;
tdmspacegroup[theta_]={tdm[theta],{-1,1,-1}*tdm[theta]};
```

In[8]:=
```
(*rotation along the long axis of a crystal can be
introduced by a counter-clockwise rotation of unit
cell's TDMs/MARVs by angle gamma around x axis*)
tdms[theta_, gamma_] = Table[
RotationMatrix[gamma*Pi/180, {1, 0, 0}]
.tdmspacegroup[theta][[i]], {i, 1, N}];
```

In[9]:=
```
(*rate of fluorescence: for 1P absorption is proportional
to cosine to the second power, for 2P absorption is
proportional to cosine to the forth power; no rotation
along the long axis of the crystal is introduced, gamma=0*)
k = 2;
F[alpha_,theta_] =
Sum[(e[alpha].tdms[theta, 0][[i]])^k, {i, 1, N}];
```

In[10]:=
```
(*ratio of fluorescence when vector e is parallel to the
long axis of the crystal to fluorescence when vector e is
perpendicular to the long axis of the crystal is a function
of angle theta*)
r[theta_] = F[90, theta]/F[0, theta];
```

In[11]:=
```
(*experimentally obtained mean value of r for 1P
absorption of mixed mTurquoise FP crystals at
488nm excitation wavelength*)
rexp = 5.13;
roots = Table[0, {i, 2}];
(*starting point for the FindRoot function*)
thetastart = {5, 70};
For[i = 1, i < 3, i++, roots[[i]] = (theta /.
FindRoot[r[theta] == rexp, {theta, thetastart[[i]]}]);
roots
```

Out[11]= {5.01424, 67.3528}

A.5 Non-fluorescent mutant of mTurquoise FP

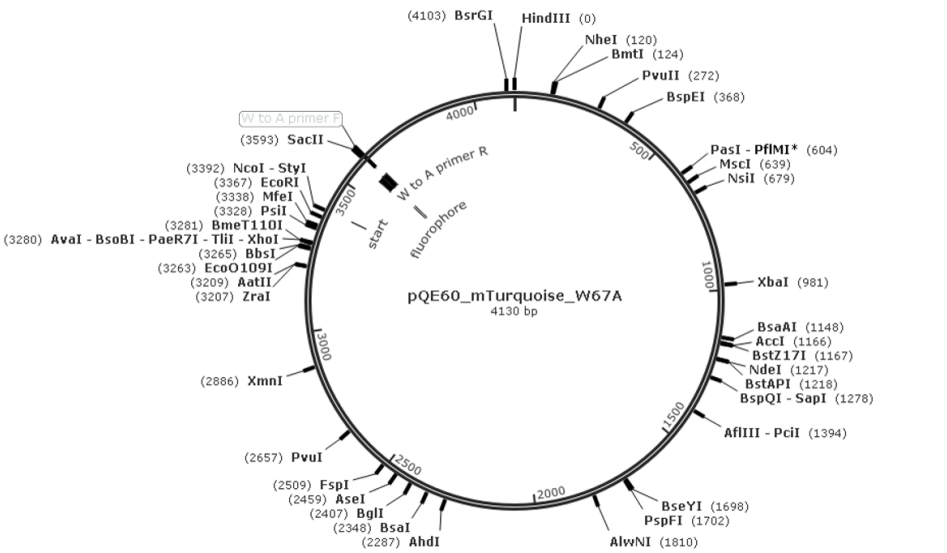

Figure A.1: Map of the mutant mTurquoiseW67A plasmid. After ligation, mutant colonies were selected by digestion of ligation product with EcoRI and HindIII restriction enzymes. Upon digestion, desired circular plasmid would get cut into two linear pieces of DNA (of 763 bp and 3367 bp lengths). These linear pieces of DNA were detected using agarose gel electrophoresis. Then, selected ligation products were sent for sequencing for final analysis. This image was created in the SnapGene software.

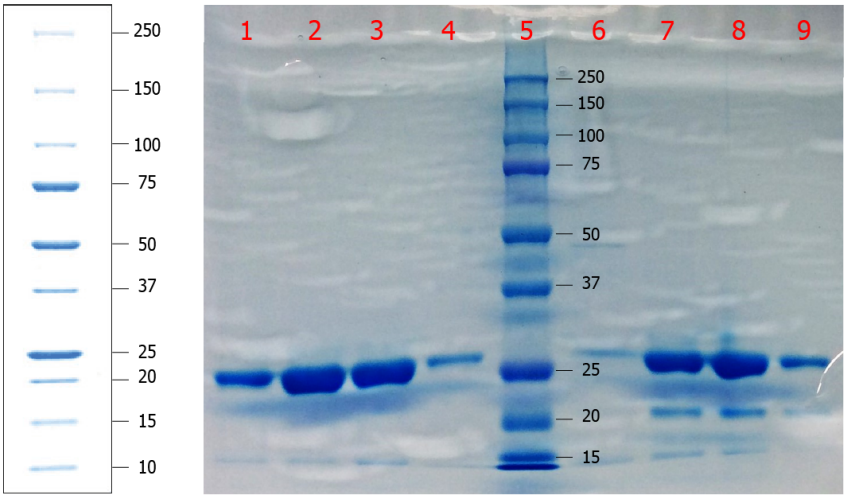

Figure A.2: Example of an SDS-page gel. SDS-PAGE was used upon protein purification for analysis of collected fractions. Here, wells 1÷4 contain mTurquoise FP fractions, wells 6÷9 – mutant mTurquoiseW67A protein fractions. Protein molecular weight marker (Precision Plus Protein Standard, BioRad) was loaded into the 5th well. Black numbers give protein molecular weight in kDa.

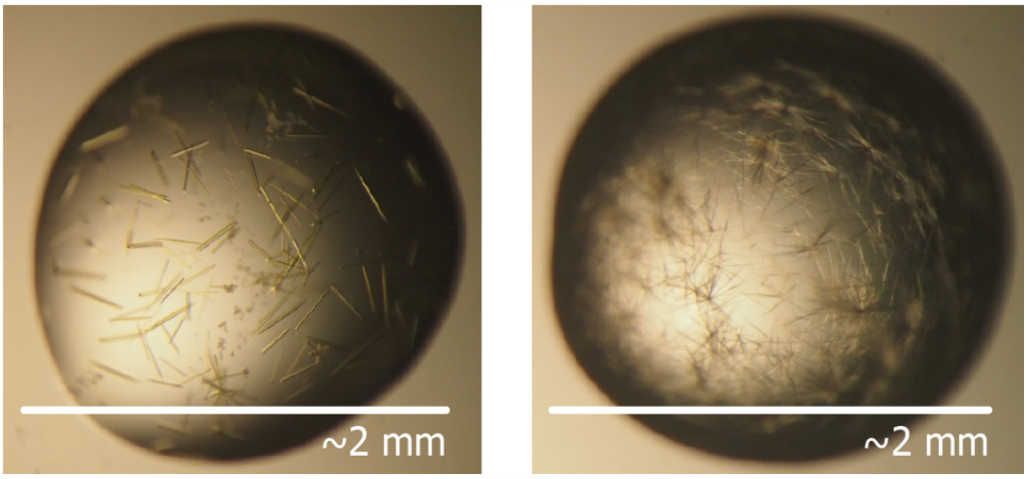

Figure A.3: Images of crystallization drops with normal mTurquoise (left) and *mixed* mTurquoise (right) FP crystals. These crystallizations were set up at the same time using identical crystallization conditions. Images shown were acquired two weeks later. We can see that *mixed* mTurquoise FP crystals are much smaller than normal mTurquoise FP crystals at the moment of acquisition. It took a sufficiently longer time (over several months) for the *mixed* crystals to reach the size suitable for polarization microscopy measurements.

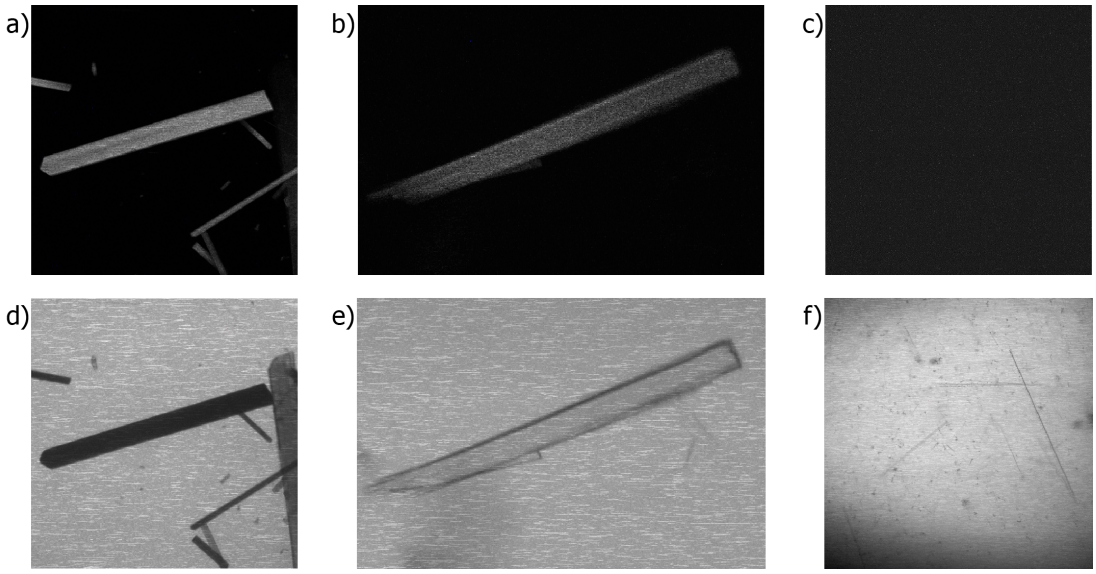

Figure A.4: a), b), c) Images of mTurquoise, *mixed* mTurquoise and mutant mTurquoiseW67A protein crystals respectively acquired in fluorescence channel (with the same intensity of the excitation light and the same detector gain). d), e), f) Images of mTurquoise, *mixed* mTurquoise and mutant mTurquoiseW67A protein crystals respectively acquired in transmission channel. We can see from images d) and e) that normal mTurquoise FP crystals absorb incident light much stronger than the *mixed* crystals. Thin, needle-like crystals of pure mutant mTurquoiseW67A protein are visible at the transmission channel (f), but do not give rise to a detectable signal in the fluoresce channel (c).

A.6 Additional X-ray diffraction measurements

More accurate X-ray diffraction measurements in terms of crystallographic axes orientations with respect to the macroscopic environment were performed with the help of our colleagues from P. Rezacova group at the IOCB Prague at the in-house diffractometer setup (for detailed description see *X-ray diffraction measurements*). Schematic representation of the setup is shown at the Figure A.5.

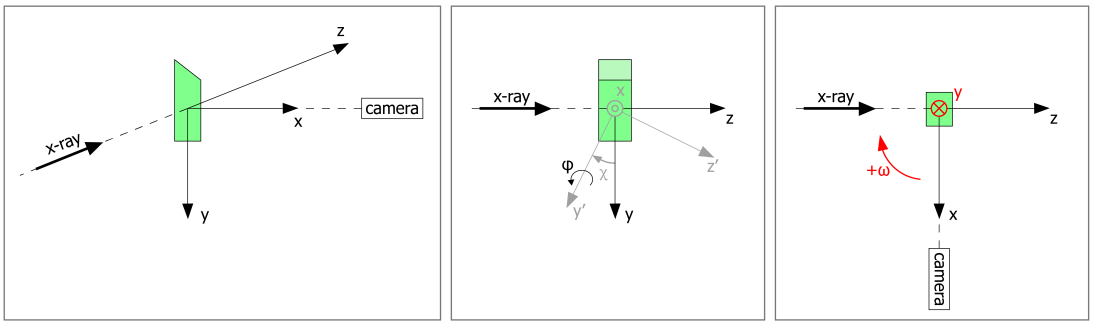

Figure A.5: A diagram of experimental X-ray diffractometry setup used for axes orientation determination. Here we assume that crystal is positioned at the origin of the xyz coordinate system shown in the picture. X-ray beam was going along the x axis. FP crystal was mounted on a holder (not shown, parallel to the y axis) and cooled with liquid nitrogen (not shown). A camera was installed orthogonally to the X-ray beam, facing x axis. Position of a FP crystal was then given by three angles, $\{\chi, \phi, \omega\}$, where $\chi \in [0°, 60°]$ corresponds to the rotation of the crystal along x axis, $\phi \in [0°, 360°]$ corresponds to the rotation of the crystal along the new y' axis and $\omega \in [-180°, +180°]$ corresponds to the rotation of the crystal along the old y axis.

All measurements have been performed in three consequent steps. First, we would run two quick measurements of a freshly installed crystal at positions $\{0, 0, 0\}$ and $\{0, 0, 90\}$. This would allow us to preliminarily determine crystallographic space group of the crystal, orientations of crystallographic axes a, b, c (in terms of angles $\{\chi, \phi, \omega\}$) and their lengths. At that point, we can already make a guess on how the axes are oriented within the crystal. However, in order to confirm that information and get structural information on FP, we would run a longer, more accurate measurement. With the approximate information in mind, we would orient the crystal in such a way that none of the crystallographic a, b, c axes coincide with the rotation axis (the axis of the mount), and start a 180° measurement with a 0.2° increment and 20 ms exposure time. This measurement would allow us to verify if our proteins are the same as the published molecular structures and would give us accurate orientations of axes in terms of angles $\{\chi, \phi, \omega\}$. Finally, in order to determine orientations of crystallographic axes with respect to the macroscopic environment, we would take pictures of the crystal with sequentially each of the crystallographic axes pointing towards the camera. Since the camera and the X-ray beam are orthogonal to each other, we would need to change crystal position from $\{\chi, \phi, \omega\}$ to $\{\chi, \phi, \omega - 90\}$ prior to taking a picture. Then, by visually analysing acquired images, we would determine orientations of crystallographic axes with respect to the macroscopic environment.